2022-12-01

Spectroscopic Study of Bi5Ti3FeO15 Aurivillius Compound for Multifunctional Applications

Mariana Castellanos
University of Texas at El Paso

SPECTROSCOPIC STUDY OF $Bi_5Ti_3FeO_{15}$ AURIVILLIUS COMPOUND FOR MULTIFUNCTIONAL APPLICATIONS

MARIANA CASTELLANOS

Master's Program in Physics

APPROVED:

Felicia S. Manciu, Ph.D., Chair

Harikrishnan S. Nair, Ph.D.

Emil D. Schwab, Ph.D.

Israel Martinez Vital, Ph.D.

Stephen L. Crites, Jr., Ph.D.

Dean of the Graduate School

Dedication

To my loving husband Joshua and my supporting parents and sisters whom I love.

SPECTROSCOPIC STUDY OF $Bi_5Ti_3FeO_{15}$ AURIVILLIUS COMPOUND FOR MULTIFUNCTIONAL APPLICATIONS

by

MARIANA CASTELLANOS

THESIS

Presented to the Faculty of the Graduate School of

The University of Texas at El Paso

in Partial Fulfillment

of the Requirements

for the Degree of

MASTER OF SCIENCE

Department of Physics

THE UNIVERSITY OF TEXAS AT EL PASO
December 2022

Acknowledgments

I would like to convey my deepest appreciation to everyone on my committee. First, I extend my deepest gratitude to Dr. Felicia Manciu for providing me with encouragement and patience throughout the project. Dr. Manciu's unparalleled support and extensive knowledge have guided me through these past years. I also had the great pleasure of working with Dr. Nair, who was instrumental in providing the samples for me to conduct this study. I gratefully acknowledge the assistance of Dr. Schwab, who has taken the time out of his schedule to aid me in this development. I would like to recognize the effort that I received from Dr. Martinez in taking part in this procedure and providing his valuable experience.

I will also take the time to thank my husband, Joshua, for his support and encouragement these past years. Thank you to my parents and my sisters for giving me the tools to continue with my career. I am grateful to all my friends and family who have taken a part in sharing this experience with me.

Table of Contents

Chapter 1 – Introduction

1.1 Introductory remarks

A growing interest in ferro electromagnetic materials has increased over the years due to the possibilities and advances it will contribute to the industrial and research fields. These materials are applied explicitly to magnetoelectric devices, including those critical to building different types of memory elements. This advancement can be possible due to both ferroelectric and antiferromagnetic ordering existing simultaneously [1]. Bismuth iron titanate ($Bi_5Ti_3FeO_{15}$) is represented by these characteristics, making it a ferro electromagnetic material known as multiferroic. Multiferroic substances are of extreme significance since they carry the potential to be used in the electronics industry as well as in electrical engineering.

A study by Mazurek et al. expands on the magnetic properties of $Bi_5Ti_3FeO_{15}$ [1]. Their preparation consists of mechanical activation, a high-energy ball milling process where elemental precursors are repeatedly fragmented, flattened, welded, and fractured. This technique was used in hopes of allowing the preparation of $Bi_5Ti_3FeO_{15}$ to reach the industrial scale making the material accessible to more developments. It was then concluded that mechanical activation is a more straightforward method for obtaining the material, yet the milling product still required thermal treatment to complete the reaction. The process to produce $Bi_5Ti_3FeO_{15}$ must still be improved and investigated to implement it in future productions.

A review article conducted by N. A. Spaldin and R. Ramesh investigates the uses and characteristics of multiferroics as they examine the advances in magnetoelectric multiferroics [2]. The electric-field control of magnetism is one of the essential applications where

multiferroics are applied. Alternating the states' controls by utilizing electric fields instead of magnetic fields will lower energy requirements for manipulating magnetic states [2]. The limitation of this application consists of high temperatures compared to the study done at 100K. A second application is reviewed for the possibility of implementing multiferroics into radio- and high-frequency devices. The progress surrounding this application indicates movement toward the controllable high-frequency responses of magnetoelectric. A variation of the coupled ordering for these multiferroics has provided routes to novel devices in magnetic field sensor magnetoelectric random access memory and voltage-tunable magnetoresistance [2]. This tunability provides the opportunity to reach voltage-tunable RF or microwave devices, including filters, phase shifters, and antennas [2]. Another reviewed idea is the application of multiferroics in ultralow power logic-memory devices. The general idea is to convert spin to charge or voltage and use the multiferroic to do the opposite conversion, turning charge to spin. This process has been reported as successfully realized in a study where the inverse Rashba-Edelstein effect was implemented to complete the first part of the experiment [2]. This success gives way to the application of multiferroics in memory devices. With these possible uses and advances, the challenges and opportunities become noticeable as new studies and reviews are published.

The investigation of the magnetoelectric effect of $Bi_5Ti_3FeO_{15}$ allows for further knowledge of what this material is used for and how it can be incorporated into more advanced studies. Chen et al. published a work that shows the difference between the composite films and pure $Bi_5Ti_3FeO_{15}$ regarding its properties [3]. The composite films were prepared for chemistry solution deposition for this study, and the results were compared with the pure $Bi_5Ti_3FeO_{15}$ films [3]. Bismuth iron titanate is once again favorable for being one of the outstanding single-phase multiferroic materials because of their potential magnetoelectric coupling behaviors. It is

also indicated that $Bi_5Ti_3FeO_{15}$-based magnetoelectric composite films will produce a powerful magnetoelectric effect. Another reason this material is favorable is because of the environmentally friendly lead-free components. It was then concluded that the polarization values for composite films were enhanced more than two times its value when compared to pure $Bi_5Ti_3FeO_{15}$ films [3]. This enhancement shows that the improved ferroelectric properties of bismuth iron titanate composite films are due to the outstanding coupling between the film layers with similar structures. The work done in this published article suggests an idea to prepare magnetoelectric composite films to facilitate their applications in memory devices, spin devices, and sensors [3].

All the distinctive studies have shown their work and material being completed in different methods. More specifically, the creation of $Bi_5Ti_3FeO_{15}$ material is obtained through complex methods. A study by Rymarczyk el al. compares the properties of $Bi_5Ti_3FeO_{15}$ ceramics when obtained using two methods [4]. The first method, known as solid-state reaction, consisted of synthesizing the refined pressed mixture of Bi_2O_3, TiO_2, and Fe_2O_3 simple oxides, which was conducted at 800°C for 5 hours. This reaction follows the following equation

$$5Bi_2O_3 + 6TiO_2 + Fe_2O_3 \rightarrow 2Bi_5Ti_3FeO_{15}$$

Where the structure for $Bi_5Ti_3FeO_{15}$ can be seen below in Figure 1. The schematic represents the oxygen atoms as yellow spheres in both the perovskite and fluorite layers. The green and blue spheres depict the bismuth atoms throughout the structure. The red spheres contained at the center of the yellow octahedra correspond to the Fe/Ti atoms, which are distributed in a disorderly pattern where the ratio of Ti to Fe atoms is 3:1.

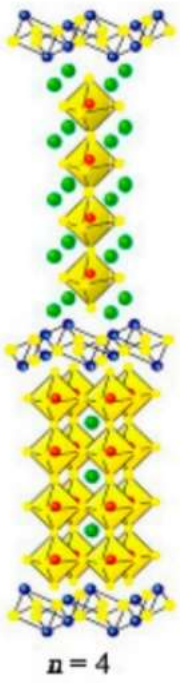

Figure 1.1: Aurivillius-type structure of $Bi_5Ti_3FeO_{15}$ [5].

Figure 1.1 shows the four-layered perovskite structures. Fluorite-like bismuth-oxygen layers are shown to alternate with these four perovskite-like layers [5]. Following the reaction, the synthesized powders were pressed in the shape of disks and compacted by a combination of free sintering and hot pressing [4]. The resulting $Bi_5Ti_3FeO_{15}$ ceramic had a symmetry of an orthorhombic system. It was determined that the hot pressing method enabled a single-phase multiferroic $Bi_5Ti_3FeO_{15}$ ceramic with higher density than the free sintering process [4]. The classification of multiferroic is furthermore proven to apply to $Bi_5Ti_3FeO_{15}$ due to the presence of both ferroelectric and magnetic properties in the original magnetizations curve.

1.2 Material constituent overview

1.2.1 Bismuth oxide and its technological applications

As the properties of $Bi_5Ti_3FeO_{15}$ and multiferroic material are studied, a deeper breakdown of bismuth iron titanate must be included. The production of this material varies from published work, yet it is found to be made from three simple metal oxides. These include bismuth oxide (Bi_2O_3), titanium dioxide or titania (TiO_2), and iron oxide (Fe_2O_3). Multiple studies have been made dealing with Bi_2O_3 and its applications. Due to the high electrical resistance and the increase in resistance when placed in a magnetic field, bismuth oxide nanoparticles have been studied across multiple fields. One study on Bi_2O_3 published by Laurent el al. discusses the well-known material's high oxygen ion conductivity due to its crystal structure and high ratio of oxygen vacancies [6]. Bismuth oxide has overall four main crystalline structures which display different electrical behaviors. These four phases are divided into thermodynamically stable, monoclinic (α) and defect-fluorite cubic (δ) phases, or metastable phases, tetragonal (β) and body-centered cubic (γ) phases [7]. Studies of each structure have been applied due to their unique properties, where Bi_2O_3 has been used as the basis for many research topics.

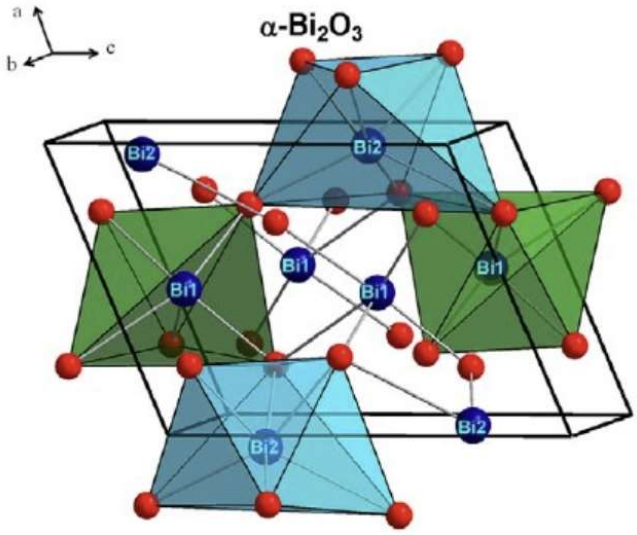

Figure 1.2: Unit cell of γ- Bi_2O_3 [8].

Figure 1.2 shows the monoclinic structure of α-Bi_2O_3 found at ambient pressure, where bismuth atoms are shown as blue spheres and oxygen as red. Regarding the phases, temperature and ambient conditions are essential for the stability of each one. The $\alpha - Bi_2O_3$ phase is stable from room temperature to 730 °C and δ- Bi_2O_3 from 730 °C to the melting point, 830°C. The transformation temperatures for the other two phases depend on the rate of cooling or heating, as well as ambient conditions and oxygen concentration [7]. The use of Raman spectroscopy can aid in identifying which structure is present in the bismuth oxide sample.

The functions of Bi_2O_3 are vast, including sensing materials, electronics, biomedical uses, and the basis for glasses. In a published work by Thomas Maeder, bismuth oxide-based glasses are reviewed for use in electronics and related applications. The primary motivation of this article is the use of nonleaded materials, which appear harmful to the environment. Bismuth oxide is favored for glass making due to its similar properties to lead when forming the glass, matching the lowest processing temperature as lead-based glasses without reducing durability and stability [9]. Combining bismuth and lead in creating heavy glasses becomes helpful in multiple fields, including optics, superconductors, nuclear technology, and specific Bi_2O_3-containing crystalline compounds [9]. Bismuth oxide has been used for multiple applications in the past years regarding scientific advancement in the industrial and research fields.

1.2.2 Titanium dioxide and its technological applications

Another component used in the production of $Bi_5Ti_3FeO_{15}$ is titanium dioxide (TiO_2), also known as titania. With a high melting point of 1,843°C, TiO_2 can be used for UV-resistant material, breaking down organic contaminants and germs, cosmetics, and paper manufacturing.

Titanium dioxide has been widely studied as a photocatalytic material for decomposing contaminants in the air and water due to its properties such as solar energy conversion, environmental applications, chemical stability, low cost, and non-toxicity. An article published by Gupta and Tripathi reviews TiO_2 nanoparticles for the ongoing climate change problem [10]. Titanium dioxide nanoparticles have been studied for photocatalytic applications, decomposition of organic compounds, and production of H_2 as fuel using solar energy [10]. The authors review the structure and electronic properties of TiO_2 and compare it with other common semiconductors used for photocatalysis. It is also discussed which enhancement will increase the photocatalytic characteristics of TiO_2 to treat water waste and pesticide degradation. First, the structure of TiO_2 is broken down into its four commonly known polymorphs found in nature, anatase, brookite, rutile, and TiO_2 [11,12]. Figure 1.3 shows the unit cell structure of the rutile phase of TiO_2. The investigation found that photocatalysis could be used as a route for selective synthetic transformations or as an advanced oxidation process for environmental cleanup [11]. This cleanup includes air purification, water disinfection, and hazardous waste remediation. The advancement in the use of TiO_2 demonstrates that renewable and clean energy technologies are anticipated.

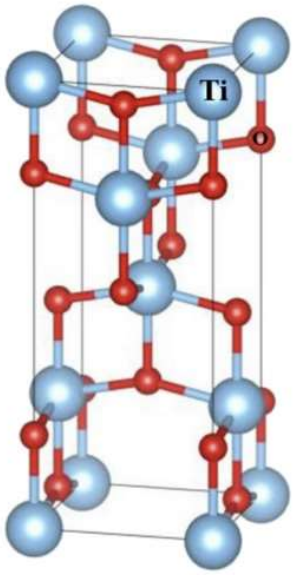

Figure 1.3: Unit cell structure of anatase TiO_2 [13].

Figure 1.3 shows the tetragonal structure of the rutile phase, which is stable at most temperatures. Rutile is also stable at pressures up to 60 kbar and particle sizes greater than 14 nm. Anatase, on the other hand, is more stable than rutile at 0 K. It similarly contains a tetragonal structure where the distortion of the TiO_6 octahedron is vaguely larger [12]. The brookite phase of TiO_2 has an orthorhombic crystal structure which is formed by edge-sharing TiO_6 octahedra. Each structure is favorable for different applications, with anatase having the highest photocatalytic activity [12].

Another study by Adawiya el al. aims to take advantage of the properties of TiO_2 in a way that would be applied to environmental settings. Thin layers of TiO_2 were prepared as part of the experiment with high photocatalytic activity and antibacterial properties to create a self-cleaning and transparent coating that could potentially be applied to outdoors windows [14]. Humanity's significant problems include air and water pollution, which has caused irritations, toxic effects, and various respiratory and skin diseases. In this study, it has been shown that TiO_2

can act as a sustainable and environmentally friendly alternative to clean up potential contamination. The research done on photocatalysts has shown that the decomposition of organic contaminants can be obtained by using clean solar energy and not having any harmful by-products [14]. The most critical aspect of this photocatalytic experiment involves the interaction between semiconducting materials and direct light from the sun. This interaction is ideal due to the implementation of solar light energy as a resource for cleaning up the environment. The experiment results showed that anatase and rutile are effective against the bacteria tested on the surfaces of these photocatalysts. It was concluded that both bacteria samples were ultimately killed under sunlight irradiation showing good photocatalyst activity and antibacterial properties for self-cleaning surfaces [14].

In addition to the environmental applications, TiO_2 has been researched for its medical use. An article published by Jafari et al. reviews the applications and effects of using TiO_2 in the medical field [15]. The advances in numerous fields, such as medicine, energy, and biosensing, have motivated the writer to review many ways TiO_2 has made an appearance in each field. Accordingly, this research shows how TiO_2 can be implemented in drug delivery, antibacterial devices, implants, and biosensors. Using TiO_2-based drug delivery systems for cancer treatment is one of the focuses of this article. The recent advances in nanotechnology in cancer treatment have surfaced due to the popularity and preference over traditional chemotherapy agents, which cause severe side effects [16]. The main goal of nanotechnology in recent years has been to deliver and release drugs while enhancing the therapeutic effects and decreasing the dangerous effects. Since TiO_2 nanostructures have high biocompatibility, controlled drug-releasing ability, and low toxicity, it is considered for application in clinical therapeutic processes. An experiment conducted by Q. Li, tested the usage of TiO_2-based nanostructures for targeted drug delivery as

cytotoxic chemo agents are loaded onto them to increase efficiency in the treatment [17]. Targeted drug delivery is necessary for reducing the damage done to neighboring cells and minimizing the anticancer drug's toxicity. Besides targeted drug delivery, controlled drug release has been studied for cancer treatment. Light has been examined as an external stimulus for the release of the drug from the delivery system, and TiO_2 nanostructures have gained attention as photoactive drug delivery carriers. The desired characteristics for this delivery system are included in the properties of TiO_2 nanostructures, such as high surface area, stability, availability, and possibility for surface modification [18].

Furthermore, TiO_2-based antibacterial devices have been used and studied to prevent and treat infections. A study by A. Besinis discusses the advantages of using metal oxides as effective microbicide agents, which improve safety and stability compared to other organic antimicrobial agents [19]. The photocatalytic properties of TiO_2 are the main reason this material is studied as an antibacterial device which has often shown inhibitory activity in different experiments. Recent developments in the biomedical applications of TiO_2 antibacterial properties have ranged from dentistry implants to medical and hospital devices [19]. Dental titanium implants are suitable for controlling infection since they provide antibacterial function and can increase implant efficiency to prevent tooth decay [19]. The disinfection of medical devices has been a severe challenge once bacteria inhibit the surfaces. Most traditional disinfection methods have been less effective than photocatalytic methods. The review mentions how TiO_2-coated surfaces are favored for deactivating the most common bacteria found in medical devices over time when exposed to UV light.

Following the discussion of the different applications of TiO_2, a study done by H. Wang goes over the necessity for TiO_2-based implants. Bone is one of the most common transplant

tissues, with surface properties and composition being the main focus for finding artificial implant material [20]. Drug-releasing implants are additionally mentioned as a result of implant surgery for a more suitable and directed drug delivery. This drug delivery system would be ideal for minimizing drug concentration while simultaneously decreasing side effects.

Biosensors based on TiO_2 became a topic of interest due to their unique properties, such as small size and ample surface area to volume ratio. This development is essential for the detection of biological analytes, which leads to the possibility of further investigating the process dealing with how to monitor patients and their response to medical or surgical therapy [21]. A suitable biosensor should have inexpensive, user-friendly, sensitive, accurate, fast, and easily manufactured properties for better efficiency and applications.

Titanium dioxide nanostructures have also been tested and used as detecting devices for humidity, oxygen, and hydrogen sensors [22]. Although these advances show promising application in the biomedical field, many improvements and further research is needed to make this metal oxide a more efficient material.

1.2.3 Iron oxide and its technological applications

The last component used to create $Bi_5Ti_3FeO_{15}$ is iron oxide, Fe_2O_3. With a melting point of 1566°C, Fe_2O_3 nanoparticles have been included in the production of coatings, plastic, nanowires, nanofibers, and targeted delivery vehicles. Shahrousvand et al. published an article where it is discussed how iron oxide nanoparticles could be used in magnetic recording, magnetic sensing, catalyst, drug delivery systems, MRI, and cancer therapy [23]. The ability to use this oxide for the mentioned areas is due to its unique characteristics, including superparamagnetic, supersaturation, and magnetic susceptibility, which come from their

magnetic properties. This study shows that the presence of iron oxide nanoparticles affects the properties of polyurethane nanocomposites making this combination a potential choice for cell therapy and tissue engineering, including nerve repair [23].

Some of the applications of this material in the biomedical field are reviewed by Arias el al. [24]. The characteristics of iron oxide, such as superparamagnetism, size, and the possibility of pairing with a biocompatible coating, are all attributed to the benefits and interest in using the material for medical applications and biotechnological advances. Many studies focus on reducing drug concentration and toxicity while increasing the effectiveness of iron oxide nanoparticle-based treatments and decreasing other side effects [24]. Iron oxide is coated and bound by drugs to improve the delivery and effects of the treatment.

Iron oxide nanoparticles are coated with different drugs to improve their stability, biodistribution, and biocompatibility [24]. Depending on what kind of drug is coated onto the nanoparticles, the effects can increase blood circulation time and the accumulation in the targeted cells or organs. Drugs bound to the nanoparticles aim to improve their pharmacological properties as iron oxide nanoparticles carry anticancer, alternative, immunosuppressive, anticonvulsant, anti-inflammatory, antibiotic, and antifungal agents [24]. The magnetic characteristics of the nanoparticles play a big part in allowing the treatment of targeted areas to perform when anticancer drugs are being delivered. This drug-delivery process is one of many ways that the properties of nanoparticles are implemented in treatments and biomedical applications. The potential of this material is still being explored as more capabilities of iron oxide are studied to overcome physical barriers and produce fine particles with precise stability, biocompatibility, and bioavailability. The structure of Fe_2O_3 is represented below.

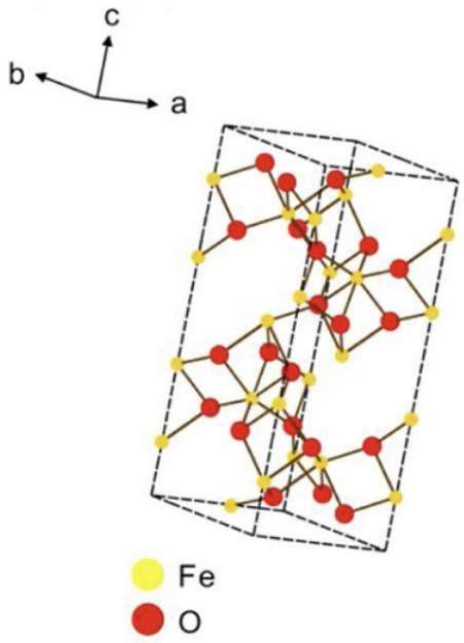

Figure 1.4: Schematic representation of the crystal structure for hematite, α- Fe_2O_3 [25].

Figure 1.4 shows the most common polymorph and most stable iron oxide known as hematite. The iron and oxygen atoms are depicted as yellow and red points, respectively. This phase contains a rhombohedrally centered hexagonal structure, different from the second most common polymorph, maghemite, with a cubic crystal structure [25].

While independently, these oxides have been intensively studied and implemented in a variety of aspects, such as medical, industrial, and engineering fields, their combination also opens new avenues for more reliable and accessible materials with enhanced properties. The focus of this research work is assessing their structural properties from a spectroscopic perspective. Understanding their properties at a molecular level is of relevance if new devices are envisioned in the future. The theoretical and experimental set-ups employed in the current analysis will be discussed in the next chapter, followed by the results achieved. Concluding remarks and future directions will also be included.

Chapter 2 – Methodology and Experimental Set-ups

2.1 Introduction to Raman Spectroscopy

2.1.1 Brief History

A brief introduction to the origin of the Raman effect and its use is essential to understand Raman spectroscopy. Sir Chandrasekhara Raman first discovered the Raman effect in 1928 [26]. Initially, the experiment included filtered sunlight beams as the light source to excite the sample. Also, his eyes were serving as the detector. He was looking for frequency-shifted light. Today's methods include using lasers instead of filtered light beams, as conducted by Sir Raman. The first laser was developed later, in 1960, by Maiman, although the theory behind it was developed in 1923 by A. Smekal [27].

The gradual improvement of the Raman instrument was developed throughout the year. Researchers concentrated on developing different lamps, starting with the excitation source. These lamps contained various elements such as helium, zinc, lead, and many others [26]. This development led to the implementation of lasers into the system in 1962 [26]. As for the detection system, improvements and new developments were seen after World War II. The earliest documentation of a photoelectric Raman instrument was from 1942 by Rank and Wiegand [26]. Later, a photoelectric instrument was developed with a photomultiplier as the detector. All the contributions and advances in the system have collectively contributed to forming commercial Raman instruments that are now used in research.

2.1.2 Theoretical background

The classical approach relies on the structure of the compound. The bonds between atoms are considered to act as springs that follow Hooke’s law. Raman studies the vibration of the

molecule, specifically the vibrational frequency. A simple diatomic molecule is considered as a mass on a spring where atomic mass, displacement, and bond strength characterize the molecule. By using approximation, the displacement can be expressed through Hooke's law as [28],

$$\frac{m_1 m_2}{m_1+m_2}\left(\frac{d^2x_1}{dt^2}+\frac{d^2x_2}{dt^2}\right) = -K(x_1 + x_2) \tag{2.1}$$

By substituting $\left(\frac{m_1 m_2}{m_1+m_2}\right)$, the reduced mass, with μ and total displacement $(x_1 + x_2)$ with q, the equation changes to

$$\mu\frac{d^2q}{dt^2} = -Kq \tag{2.2}$$

Solving equation (2.2) for q results in

$$q = q_0 \cos(2\pi\nu_m t) \tag{2.3}$$

Here, ν_m is the molecular vibration and can be represented as,

$$\nu_m = \frac{1}{2\pi}\sqrt{\frac{K}{\mu}} \tag{2.4}$$

Equation (2.3) shows that the molecule vibrates in a cosine pattern. Additionally, equation (2.4) shows how the frequency is proportional to the bond strength and is inversely proportional to the reduced mass [29]. Since the bond strength and reduced mass varies based on the molecule, it can be inferred that each molecule will have its unique vibrational signature [29].

Knowing that the polarizability of a molecule is given by a function of displacement, vibrational frequencies can be measured through the Raman effect. The incident light interacts with a molecule, inducing a dipole moment, P, which is equal to the product of the molecule's polarizability and the incident light's electric field [28]. Taking the light source as an electromagnetic wave with an electric field of frequency υ_0, its interaction with the molecules causes a periodic movement with a similar frequency. This oscillation causes an induced dipole where the charges are separated within the molecule. The oscillating-induced dipole becomes a

source of electromagnetic radiation, which constitutes scattering light. Raman effect occurs where the scattered light is represented by frequencies that are not equal to that of the incident light, also referred to as inelastic scattering [30].

The theory follows such interaction between the electromagnetic wave and the material's induced dipole. The following relationship represents the dipole moment:

$$P = \alpha\vec{E} \tag{2.5}$$

where α represents polarizability and $\vec{E}$ is the electric field corresponding to the incident electromagnetic wave. Polarizability solely depends on the molecular structure and bonds, making it a material property, whereas the electric field is denoted as

$$\vec{E} = E_0 \cos(2\pi\upsilon_0 t) \tag{2.6}$$

where υ_0 belongs to the frequency of the electromagnetic incident wave, $\upsilon_0 = \frac{c}{\lambda}$. The time-dependent induced dipole is given by the substitution of equation (2.6) into (2.5), as seen below:

$$P = \alpha E_0 \cos(2\pi\upsilon_0 t) \tag{2.7}$$

Applying small amplitude approximation to represent polarizability as a linear function of displacement will result in the equation,

$$\alpha = \alpha_0 + q \left(\frac{\partial\alpha}{\partial t}\right)_{q=0} + \cdots \tag{2.8}$$

When combined with equations (2.3) and (2.7), the result is given by,

$$P = \alpha_0 E_0 \cos(2\pi\nu_0 t) + q_0 \cos(2\pi\nu_m t)\, E_0 \cos(2\pi\nu_0 t) \left(\frac{\partial\alpha}{\partial t}\right)_{q=0} \tag{2.9}$$

Equation (2.9) shows that the interaction between the molecule and incident light gives way to two effects. The first term consists of the effect called Rayleigh scattering, which shows no difference in the frequency of the incident light [28]. Raman effect is seen in the second term, which can be expanded to,

$$q_0 E_0 \left(\frac{\partial \alpha}{\partial t}\right)_{q=0} [\cos(2\pi\{\nu_0 - \nu_m\}t) + \cos(2\pi\{\nu_0 + \nu_m\}t)] \quad (2.10)$$

Equation (2.10) represents a shift in the frequency of the incident light, ν_0, by plus or minus the frequency of the molecular vibration, ν_m [28]. The increase in frequency results in an Anti-Stokes shift, whereas the decrease in frequency gives a Stokes shift. Finally, the spectroscopist can directly measure the vibrational frequency of a molecular bond by measuring the difference in frequency from the incident light, typically measuring Stokes shifts.

After deriving the Raman effect using classical waves to interpret the incident light, it would be easier to depict the quantum particle interpretation. Firstly, the incident light beam will excite the electrons of the molecules, bringing them into a virtual state where they become unstable. Releasing a photon will bring the electron back to a stable energy level. The final state could be the ground state or the first excited state. This photon contains the particular energetic information of the molecule. Thus, telling if there is an energy shift between the incident and the scattered photons. This energy shift is also characteristic and unique to each molecule. The Raman scattering process is like a fingerprint for each sample. This characteristic sample information allows for the interpretation of the spectra during research.

In Raman scattering, the electrons either gain or lose energy through this process, resulting in Anti-Stokes and Stokes, which are schematically presented in Figure 1.1. This effect happens in less than 1% of the scattered light. The phonon modes are then recorded in an intensity vs. wavenumber graph.

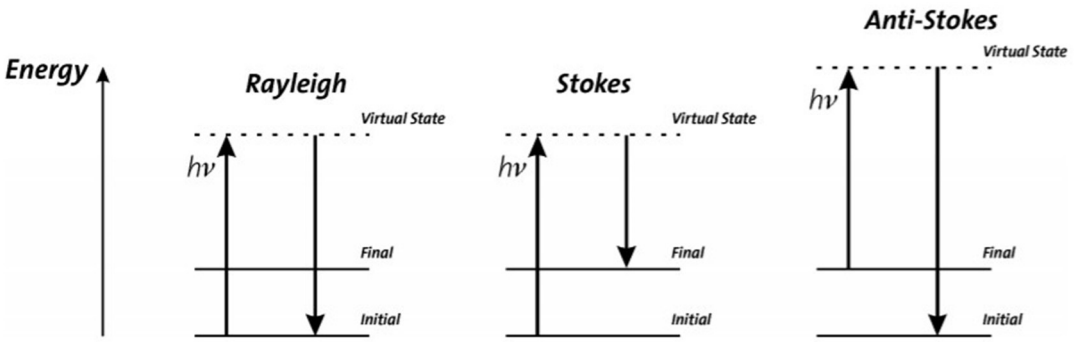

Figure 2.1: Energy level diagram of (a) Rayleigh scattering, (b) Stokes scattering, (c) Anti-Stokes scattering [27].

One of the groups includes the photons scattered with the same energy and frequency as the incident photon. In classical mechanics, this is an elastic collision between the photon and the electrons of the sample, also known as Rayleigh lines. Thus, Rayleigh scattering is also known as elastic scattering. However, the groups of interest are the photons that collide with the electrons inelastically.

During the Raman process, the photons scattered with less energy than the incident photon are the Stokes modes and produce Stokes Raman lines on a recorded spectrum. These lines indicate that the electron has lost energy through the interaction. On the other hand, the Anti-Stokes Raman lines emitted photons with higher energy values than the incident photon. Similarly, these lines indicate that the electron has absorbed energy through the interaction. The electron then releases energy in form of a photon, returning to a stable energy state. These states could differ between the vibrational ground state and an excited state.

The molecular fingerprint is different for diverse molecules. The intensity of the Anti-Stokes and Stoke lines, attributed to inelastic scattering, is much less than the elastic Rayleigh

lines. Furthermore, in Raman spectroscopy, the Stoke lines are used more in analyzing molecular sample properties.

The equation represents the energy shift relative to the excitation line (laser line):

$$\bar{\nu} = \frac{1}{\lambda_{\text{incident}}} - \frac{1}{\lambda_{\text{scattered}}} \tag{2.10}$$

Where ν is the frequency of the photon. The Raman frequency shift, $\bar{\nu}$, is commonly given in wavenumbers [27]. In the classical theory of scattering, the intensity of the scattered light is directly proportional to the power of the frequency of the incident photon:

$$I \sim \nu^4 \tag{2.11}$$

Therefore, the frequency of the light used in the experiment highly influences the intensity of the results. Even more, based on this relationship, the following equations can be derived:

$$I_{\text{Stokes}} \sim (\nu - \nu_v)^4, \text{ and } I_{\text{Anti-Stokes}} \sim (\nu + \nu_v)^4 \tag{2.12}$$

This relation assumes that $I_{\text{Anti-Stoke}} > I_{\text{Stokes}}$, but the opposite is true experimentally [31]. Since Anti-Stokes scattering requires the initial state of the electron to be already excited, it is less probable to record a photon that will have more energy than the incident photon. This result will lead to more negligible intensity levels in the Raman spectra for Anti-Stokes scattering. Stokes scattering is much more efficient in analyzing a sample, as revealed in Figure 2.2. Usually, a Raman spectrum is plotted as the intensity of the scattered light versus the energy difference in rapport to the used excitation wavelength. Also, adequate filters are employed experimentally to reduce the vigorous intensity of Rayleigh elastic scattering, which is dominant, especially for fluorescent samples. Due to the difference between the Anti-Stokes and Stokes lines, the latter would be more efficient for collecting and analyzing data.

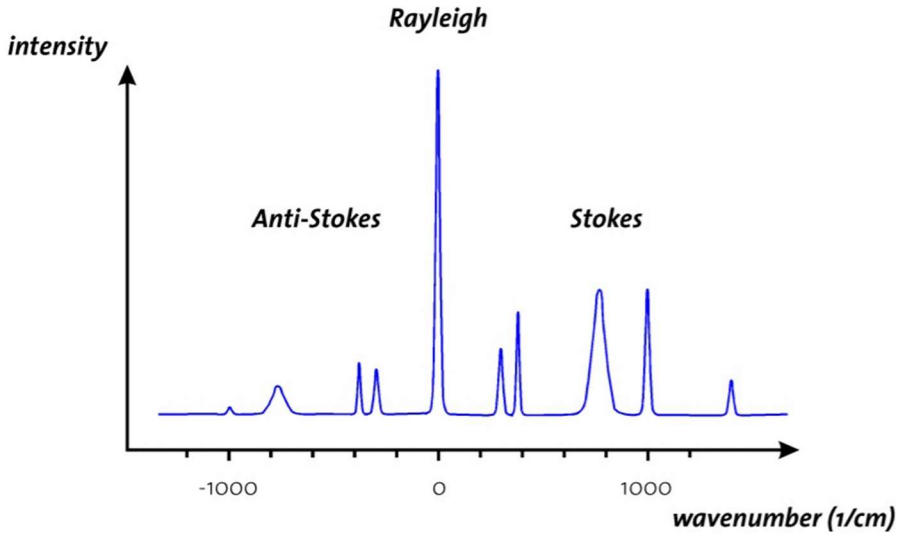

Figure 2.2: Shows a comparison between the intensities of all three types of scattering (Anti-Stoke, Rayleigh, and Stoke) [27].

2.2 Confocal Raman Microscopy

2.2.1 Principles of Confocal Microscopy

In confocal Raman microscopy, the light source is tightly focused on the sample's surface. Confocal microscopy consists of a two-lens principle set-up with a beam splitter at the center. The detector collects fluorescence, consisting of reflected light, which is focused through a small hole in the front and collected by the same objective in the system. The small hole in front of the detector is the pinhole and is part of the system set-up. The pinhole ensures that the only light detected is from the image's focal plane. By doing this, the image contrast is significantly increased. Also, by selecting a specific pinhole size, the image's resolution can increase significantly. The laser provides energy to the molecules in the sample. Figure 2.3 shows the basic set-up of a confocal microscopy system. The light source that comes from the laser is optically guided through an optical fiber to pass through an objective at the focus plane. The path of the light can be seen in

the image as it follows the green arrows. In the case of confocal Raman microscopy, the reflected light is passed through a filter, where only Raman frequencies are allowed before the detector records it.

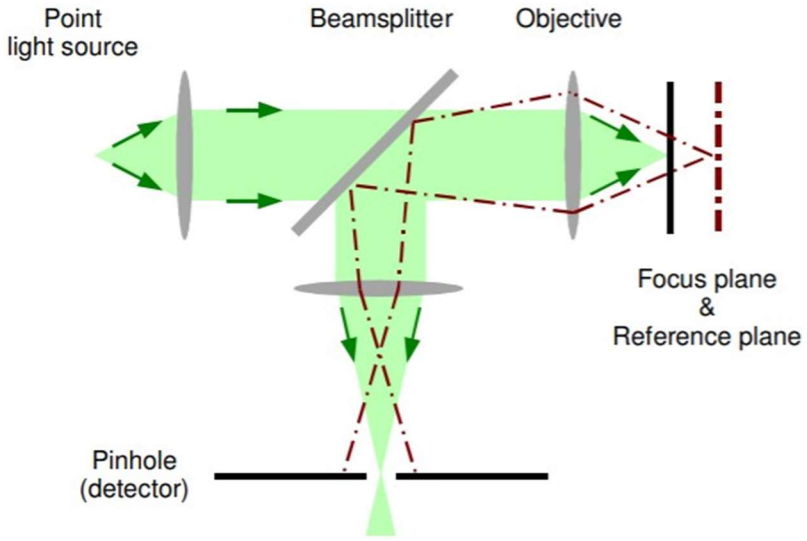

Figure 2.3: Schematic representation of the principal set-up of a confocal microscope [27].

Figure 2.4 shows the path of the light beam through the CCD. The CCD sends live broadcasts of the material to the computer for viewing the sample through the microscope. The filter and the rotational prism allow us to take spectroscopic measurements without moving the sample. This technique allows a more precise measurement of the material by presenting a sample view and showing the single spectra measured at that location.

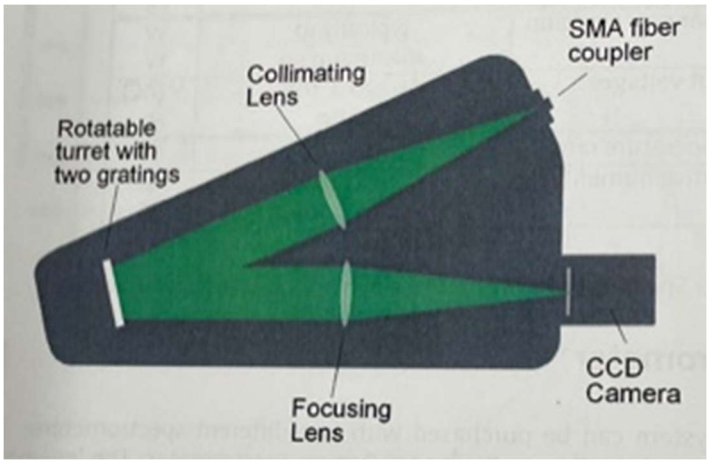

Figure 2.4: Schematic representation of a spectrometer. [27]

2.3 Raman Experimental Set-up

An *alpha 300 RAS* WITec system was used for data acquisition. This instrument is based on the previously mentioned confocal microscopy principles and also is combined with a high-efficiency spectrometer. It is ideal for high optical and spatial resolution and for delivering chemical information in the sub-micrometer regime. The light source used in the current measurements is a green light excitation of a frequency-doubled neodymium-doped yttrium-aluminum-garnet (Nd:YAG) laser at 532 nm, which can give a resolution down to 350 nm. The optical set-up and diagram is presented in Figure 2.5. It consists again of a two-lens system. In this system, a single-mode optical fiber is used as the pinhole and for delivering a laser/light source point into the sample. This specific optical fiber can only deliver a Gaussian beam, which is also known as a single transversal mode. When the light is reflected by the sample, it is collected by the objective. This light travels as a parallel beam directed toward the top of the microscope, where it is focused on a multi-mode optical fiber that connects the microscope to the CDD camera. A more detailed specification of the entire system shown schematically in Figure 2.5 is as follows: U1 is an XY positioner that is employed to align a sample in the x and y directions. This is a

component of the scan stage, which includes separate sensors at each axis as well as a piezoelectrically driven 3-axis flexure stage, U2. The objective turret with objectives is seen right above the scan stage, being labeled U3.

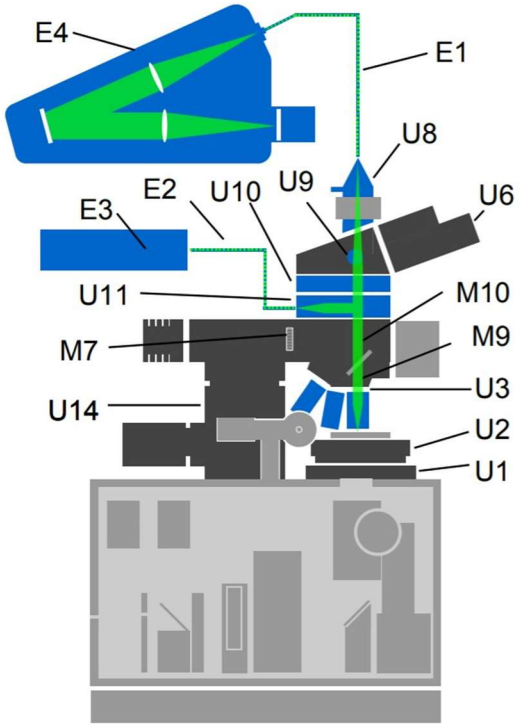

Figure 2.5: Schematic illustration of the alpha 300 confocal Raman system [27].

The binocular tube with an ocular camera, U6, helps with visualization of the sample image using a white light source, E3, prior to the collection of Raman data. A fiber coupling unit, U8, is used in coupling the optical scattered Raman output with the multimode fiber. To direct the collected laser light through the objective (E1) towards the detector, a push rod found on the side of the microscope, U9, is used. Also, a filter holder, U10, containing the appropriate filter needs to be positioned in place.

2.4 Fourier Transform Infrared (FT-IR) Spectroscopy

Fourier Transform Infrared (FT-IR) spectroscopy is often referred to as complementary to Raman spectroscopy. Raman active refers to light scattering due to the change in polarizability through vibration, whereas IR active refers to light absorption due to the change in dipole during vibration [32]. This reason is why both measurements are gathered for the experiment.

The main difference between the two techniques is that the latter employs an infrared light source, not a laser. Before FTIR spectroscopy came about, infrared radiation had to be discovered. Astronomer Sir William Herschel discovered infrared radiation in 1800 using thermometers to designate a temperature for each color present in the visible spectrum [33]. His results showed that there is a temperature increase from blue to the color red, with an additional measurement corresponding to the warmer temperature further from the red end of the visible spectrum [33]. This measurement pertained to infrared radiation, which is used today on an experimental basis.

The system consists of a Michelson interferometer, a product of the Michelson-Morley experiment [34]. This experiment was conducted to find the velocity of Earth concerning a medium in space said to carry light waves, known as hypothetical luminiferous ether [34]. A.A. Michelson first conducted this experiment in 1880-81, then it was reattempted by Michelson and Edward W. Morley in 1887 [34]. The set-up consisted of the Michelson interferometer, which compares optical path lengths moving in two perpendicular directions [34]. Fourier Transform Infrared spectroscopy simultaneously exposes a sample with multiple IR light frequencies while using an interferometer and post-processing the transmitted light [32]. For this process, an IR light passes through a beam splitter. Half of the light reaches the fixed mirror, and half will reach the moving mirror with a constant velocity, as shown in Figure 2.6 [32].

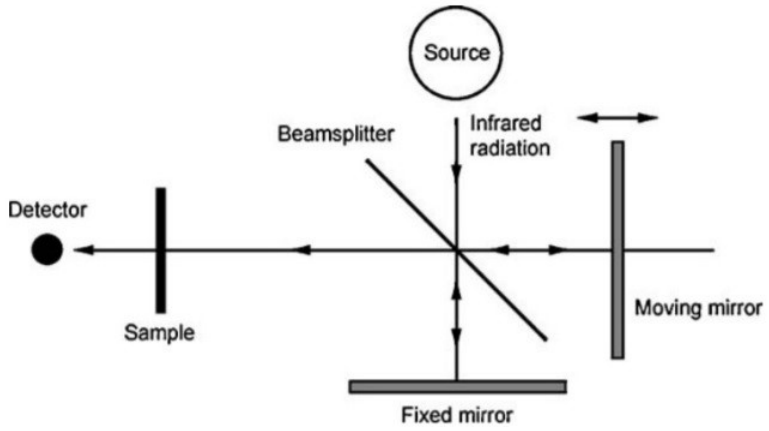

Figure 2.6: Schematic representation of Michelson interferometer [32].

The split beams are then reflected and combined to take a path different from the beams to create an interference pattern. This pattern will represent the constructive and destructive interference sent to the sample. Then, the transmitted portion is sent to a detector compared to a reference sample beam. Fourier transform is then performed to obtain the spectrum as a function of wavenumber [32]. Fourier transform is a generalization of the more complex Fourier series in the limit $L \longrightarrow \infty$ [35]. First, start with a function f(x) which will give the Fourier transform by

$$F(k) = Fx[f(x)](k) = \int f(x)e^{-2\pi ikx}dx \tag{2.13}$$

This function is used in the frequency domain representation [32]. Regarding sine, $\sin(2\pi k_0 x)$, and cosine, $\cos(2\pi k_0 x)$ functions, the Fourier transform can be used to give the following

$$\frac{1}{2}i[\delta(k+k_0) - \delta(k-k_0)], \text{ and } \frac{1}{2}i[\delta(k-k_0) + \delta(k+k_0)] \tag{2.14}$$

respectively [32]. This concept is used in image processing to decompose the image into sine and cosine components [32].

2.4.1 FT-IR Experimental Set-up

The Bruker IFS 66v, which is the system used in the current experiments, has an internal optical path, as shown in Figure 2.7. Since it is based on a Michelson interferometer, it consists of four main parts, an infrared source, a beamsplitter, and two plane mirrors. One mirror is fixed, and a second mirror is allowed to move.

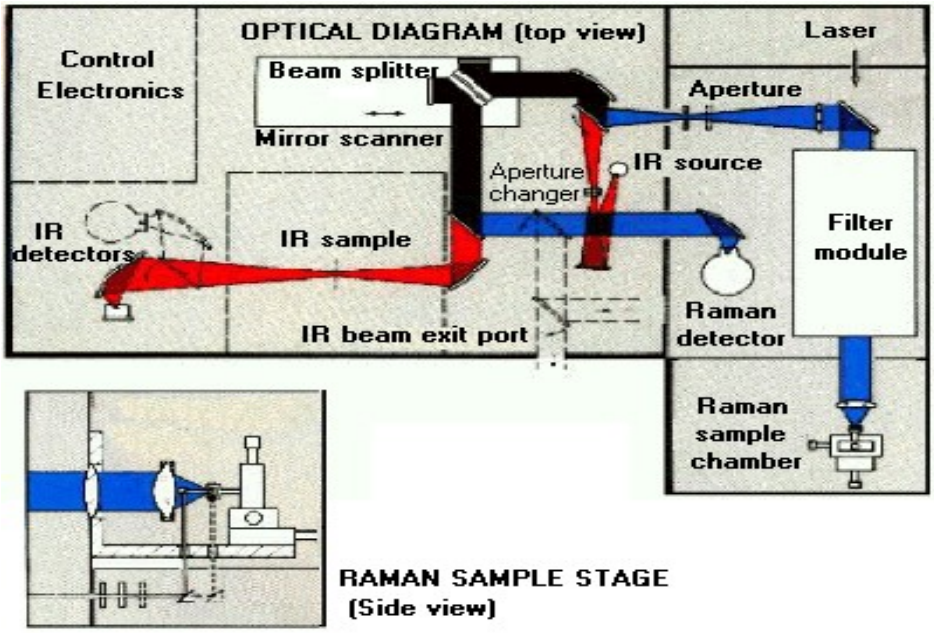

Figure 2.7: Internal optical path of IFS 66v Brucker system (courtesy of Bruker Inc.)

The parallel infrared radiation from the source travels to the beamsplitter, which is oriented at 45° and divides this light into two beams of equal intensity; one beam will be transmitted, and the other reflected. These two beams travel to the two different mirrors that are oriented perpendicular. They are reflected back by the mirrors to the beamsplitter, where they recombine. Specifically, the reflected beam reaches the fixed mirror after traveling a distance L, which is called the *physical distance*. Subsequently, the beam is reflected back to the beamsplitter and returns to it after traveling a distance equal to $2*L$, which is called the *optical path*. The transmitted beam reaches the movable mirror. If this mirror is the same distance from the beamsplitter as the fixed

mirror, the beam would have traveled the same physical distance, L, to reach it. However, as the name implies, the movable mirror travels back and forth around the distance L by an amount equal to δx. When the transmitted beam returns to the beamsplitter, it has traveled a distance of $2(L + \delta x)$. The two beams are recombined at the beamsplitter with an *optical path difference*, also called retardation, of $2*\delta x$.

The two beams can recombine by interfering either constructively or destructively, depending on the optical path difference and on the wavelength of the light as follows:

(1) Constructive interference $2*\delta x = n*\lambda$ $n = 1, 2, 3\ldots$

(2) Destructive interference $2*\delta x = (1/2)\ n*\lambda$ $n = 1, 3, 5\ldots$

Consequently, the output beam has an intensity that depends on the amount of constructive interference, varying as a function of the optical path difference and the wavelength of the incident radiation. The intensity is at a maximum when the optical path difference is zero since all wavelengths of light constructively interfere at this point, called the *zero path difference* (ZPD). The plot of detector response as a function of optical path difference is called an interferogram.

The shape of the *interferogram* dramatically depends on the characteristics of the light source. For example, the interferogram of a monochromatic source with only one wavelength would be a cosine function. The Fourier transform of this interferogram would give a single prominent peak in the final spectrum. In the case of our broadband source, which was used in the current experiments and had a continuous infinity of wavelengths, the interferogram consists of the sum of all the cosine waves that belong to each distinct wavelength present. For this type of source, only at the ZPD are all of the wavelengths in phase; this is the scenario when the interferogram will show a single maximum and some small peaks close to it. The effects of the chosen beamsplitter (which is a non-ideal crystal), detector response, and of the chosen

apodization function (which acts to remove sidelobes in the interferogram) are reflected in the shape of the typical interferogram.

2.5 Comparative Advantages and Disadvantages of Raman and FT-IR Spectroscopies

2.5.1 Advantages and Disadvantages of Raman Spectroscopy

As Raman spectroscopy grows in the research field, new advantages and disadvantages have surfaced. The advantages allow researchers to study a broad area of samples, including molecular diagnostics. This vibrational spectroscopy technique gives way to identify substances and molecular changes better. The results are also given with high spatial resolution, which is favorable in the case of imaging biological samples [36].

Raman spectroscopy is non-destructive and non-invasive for molecular diagnostics. Due to its dependence on wavelength and power, data can be collected without harming the material. In addition, sample preparation is minimal and label-free, eliminating dyes and toxic waste products from the process. This holds for cancer diagnostics, where biological samples are measured non-destructively and without labels. Optical technology advances have contributed to the advantages of Raman spectroscopy by making it possible to apply it macroscopically and microscopically. This allows the study of bulk samples in addition to the study of samples on the cellular level.

Raman spectroscopy contributes to physiological measurements due to weak water interference. This is compatible with the biological study of the function of living organisms as well as their parts [36]. Besides the applications in biology, Raman spectroscopy is also suitable for chemical analysis. It measures the quantity of a substance present in a sample as well as the classification of the substance.

The main disadvantage of Raman spectroscopy is its sensitivity to fluorescence, making it challenging to measure samples exhibiting autofluorescence. On the other hand, infrared absorption, while sensitive to water absorption, is insensitive to fluorescence. Another disadvantage of Raman spectroscopy is the weak Raman signals. This disadvantage leads to a more extended acquisition period and slower imaging when taken by point scanning. A more sophisticated data analysis is often necessary for video-rate imaging due to the low scattering efficiency and more extended measurement periods [36].

2.6 Sample preparation

The $Bi_5Ti_3FeO_{15}$ aurivillius compound was synthesized in Dr. Nair's laboratory using a solid-state reaction. Powdered samples of Bi_2O_3, Fe_2O_3, and TiO_2 were thoroughly mixed using stoichiometric proportions. The mixture was then pressed into pellets and placed into alumina crucibles. Then the sample was sintered at 1053 K for 2 h. The sintered sample was ground and pressed into pellets. The pellets were sintered at 1323 K for 2 h. Then the sintered sample was ground into a fine powder, and the preceding process was repeated until the XRD data showed no change between successive repeated processes.

2.6.1 Raman Data Acquisition

Prior to Raman spectra recording of the bismuth iron titanate and its constituents Bi_2O_3, Fe_2O_3, and TiO_2, a couple of steps must be followed to receive the best results. First, we must turn the power on, along with the WITec Control program, which will be used for recording measurements. Once the system is powered, the laser is switched on, and the process for

calibration is started. Standard calibration of the system is performed using a silicone sample under the 100x magnification objective.

2.6.2 FTIR Data Acquisition

First, $Bi_5Ti_3FeO_{15}$ and the oxides samples were prepared into pellets and placed on the sample holder. Cesium iodide is used as the matrix for these pellets, where a small portion is added to a clean agate mortar. After adding the matrix, a minor part of the sample is added before grinding with the agate pestle. Once the sample is well incorporated into the matrix, and the material looks like a powder, it is ready to be used as a pellet. Too much matrix could result in a thick sample, resulting in a small signal in the spectra. Therefore, it is ideal for working with small amounts of the matrix and sample. This procedure is repeated for each oxide and $Bi_5Ti_3FeO_{15}$. Consequently, each tool must be thoroughly cleaned before reusing it for the following sample.

After obtaining the appropriate amount of powder substance, a PIKE Technologies pellet press is used. The pellet press is ideal for making 13mm pallets which will go on the sample holder for transmission measurements. First, each part is cleaned with acetone before each use, excluding the rubber circles that will secure the parts. Once clean, the powder containing the sample is placed in the center of the pellet press. The pellet press is then assembled for the hydraulic press, which will experience a pressure of 3 metric tons.

After a couple of minutes, the pellet press is then retrieved from the hydraulic press. It is taken apart, revealing the newly formed pellet. The pellet is then removed using precision and a steady hand to keep it intact. This procedure can be repeated for the same sample as much as needed. Once a good pellet is achieved, it is placed near the system for testing and labeled with

the sample's name. This procedure is repeated with each sample, cleaning each of the parts and materials used before working with a new substance.

Now that the pellets are ready for measurements, the system is initially prepared for measuring in mid-IR. Some parts must be manually changed, such as the beam splitter. A KBr beam splitter was used along with a Globar light source for this part of the experiment. These are important for measuring in mid-IR since they are ideal for gathering wavenumbers between 400 cm^{-1} and 4,000 cm^{-1}. To change the light source, it is required to follow the steps in order.

First, the computer is turned on, and the OPUS control program is installed and ready to use. Compressed air is then provided to the system, and the pressure is observed until it reaches a steady 40 psi. This is important for the moving of the sliding mirror as well as rotating the stationary mirrors for completing the measurements in mid-IR. Once the air is at 40 psi, the IFS Electronic Unit is turned on, and MIR is selected. A whirling sound is then heard as the mirrors rotate to fit this setting. The new position of the mirrors will direct the transmitted light toward the mid-IR detectors.

The motor pump is then turned on by rotating the knob until the noise changes from the original sound and an extra turn for good measure. In addition to the manual changes, the aperture should be set at 10 mm for the rest of the measurements. For aligning the system, an empty sample holder is placed in the sample chamber. Once in place, the whole system must be placed under vacuum using the Bruker controls. Starting with the Main Menu, Vacuum Control is selected, followed by Sample Change Menu and pressing Vent Optics. This setting places the system in a vacuum by pumping out the air inside. Once ready, a signal will appear on the Bruker controls stating that the system is ready for use.

On the OPUS program, select a previous background from which the settings are copied. This can be done by selecting the "load" option and selecting OPUS data. Then, the file labeled Background is selected, opening a control page where it is renamed to fit this experiment's data. Once the name is changed under the Advanced and Basic tabs, the Check Signal tab is opened, and auto-align is selected once the signal is visible. Next, the Save Peak Position button is pressed. Going back to the Basic tab and selecting Background Single Channel will allow the system to begin the reading. The system will do a total of 256 scans through the process of collecting the Background. Once collected, the Background is loaded and saved.

Without closing the background file, the measurements of the pallets can begin. The sample chamber is then brought into atmospheric pressure once the Evacuate Optics setting is selected on the Bruker controls. This will allow for easy removal of the sample holder. On the same holder, a chosen pallet is secured. A small piece of double-sided tape is used to secure the pellet onto the sample holder, making sure that the tape is not obstructing the hole in the holder. It is also crucial that the pellet has no cracks. Once the pellet is secured, the sample holder is placed back in the sample chamber.

Once the pellet is in the sample chamber, the lid is placed back on top, and the system is placed in vacuum by selecting Vent Optics. Again, the Bruker control must read Ready before performing any measurements. With the Background selected, the Advanced Data Collection icon is pressed. Under the Basic Tab, the file is renamed to an appropriate title that includes the substance in the pellet. This is repeated under the Advanced Tab. To make sure that the Background is still selected, the Check Signal Tab is pressed. There, a signal will appear without having to press anything else. The position of the mirror and the amplitude is recorded for future reference. Next, the Sample Single Channel button is pressed under the Basic Tab. The exact

number of scans will take place, 256, before the spectra are shown. This is repeated for each pallet, making sure that the system is in vacuum for each measurement and that the Background is selected before beginning the scans.

Chapter 3 – Results and Discussion

Since the $Bi_5Ti_3FeO_{15}$ was synthesized by mixing Bi_2O_3, Fe_2O_3, and TiO_2 powder samples in appropriate stoichiometric proportions followed by sintering, an easier understanding of the compound's spectroscopic results is by comparison with the phonon modes of its constituents. Thus, below, these results are first being presented and analyzed.

3.1 B_2O_3

Bismuth oxide, a p-type, wide bandgap semiconductor (2.85 eV at room temperature in the monoclinic phase), has been used in a variety of technological applications, ranging from sensors [37-40], transparent ceramic glass [41], and optical coatings [42]. Besides the material's properties, such as high refractive index, high dielectric permittivity, and photoconductivity, Bi_2O_3 exhibits different structural polymorphs, such as α, β, γ, δ, and ω, each with different structural assets and applicability. The α and δ phases are the ones that are stable at low- and high temperatures, respectively.

The phonon modes of the stable α-phase of the material is spectroscopically analyzed in Figures 3.1 and 3.2. Bismuth oxide has a centrosymmetric structure, which not allows an exact coincidence of the IR and Raman modes. The monoclinic structure of the material belongs to $P2_1/c$ (C^5_{2h}) group. It contains 4 Bi_2O_3 per unit cell, with the twenty atoms distributed uniformity and having sixty degrees of freedom. The group symmetry predicts twenty-seven IR active modes and thirty Raman active modes. Fewer modes have been observed experimentally [43]; those from the material's irreducible representations becoming both IR and Raman active. Also, since a lower symmetry is expected in powder materials, such as those analyzed here, a likely less homogeneity in atomic bonds in all directions will contribute to a reduction in vibrational frequencies arising

from different polarizations. Consequently, similar modes will be depicted as single band measurements.

The Raman spectrum recorded at room temperature, which is presented in Figure 3.1, shows vibrational lines at 151 cm^{-1} (B_g), 184 cm^{-1} (A_g), 210 cm^{-1} (A_g), 282 cm^{-1} (A_g), 314 cm^{-1} (A_g), 410 cm^{-1} (A_g), 446 cm^{-1} (A_g), and 527 cm^{-1} (B_g). Unfortunately, due to the cutoff of the experimental band-pass filter, no phonon modes below 130 cm^{-1} could be observed. Another remark, which has also been reported in the literature [43], is the sharpness of the vibrational lines below 200 cm^{-1}, such as those at 153, 184, and 210 cm^{-1}, compared with the ones above 200 cm^{-1}, such as the bands at 282, 314, 410, 446, and 527 cm^{-1}. The low-frequency vibrational modes (below 200 cm^{-1}) are tentatively attributed to the Bi atoms movements and Bi–Bi stretching modes in the material structural subunits [44]. The vibrations observed in the frequency range from 190 cm^{-1} to 340 cm^{-1} generally correspond to bending modes of both BiO_5 and BiO_6 subunits [44,45].

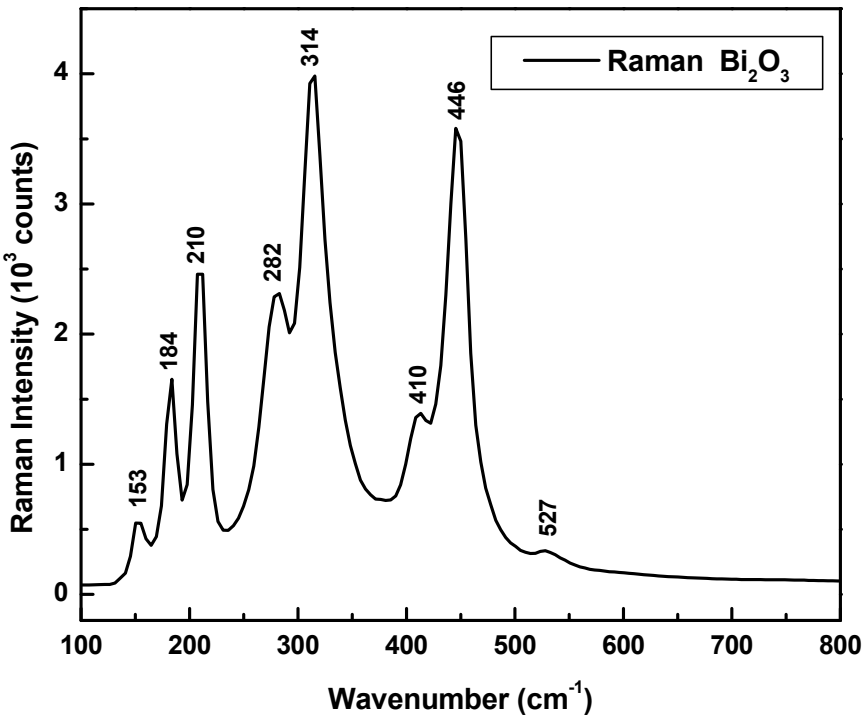

Figure 3.1: Raman spectrum of α-Bi_2O_3.

Usually, the higher frequency bands are attributed to divalent and trivalent cations, making analysis more complex. Thus, the vibrational lines at 153 cm^{-1} (B_g) and 184 cm^{-1} (A_g) are associated with Bi atoms and symmetric O atoms displacements in the lattice of the material, respectively, while the peaks at 210, 282, 314, 410, 446, and 527 cm^{-1} also have added contribution from Bi–O symmetric stretching vibrations [44,45]. The vibrational line at 446 and 527 cm^{-1} correspond to longitudinal optical (LO) and defects from oxygen vacancies and interstitial bismuth, respectively. The weak peak at 410 cm^{-1} is assigned to the second-order symmetric Raman scattering mode at the zero boundary phonon process [45].

The infrared transmission spectrum of the compound is presented in Figure 3.2. The polar character of the IR vibrations results in their further splitting into longitudinal and transversal optical components, affecting the broadening of the IR bands.

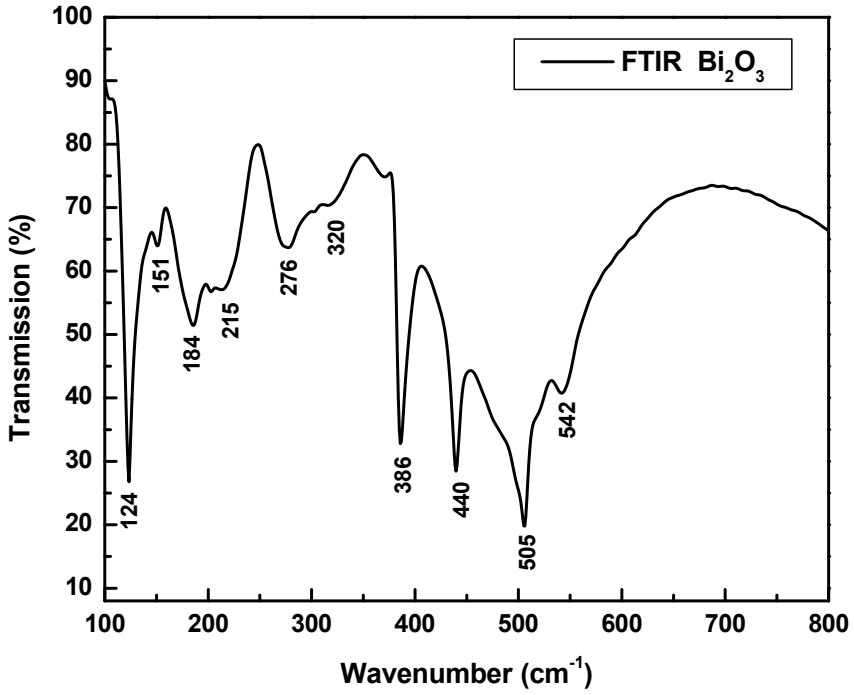

Figure 3.2: Infrared transmission spectrum of α-Bi_2O_3.

The longitudinal components are IR and Raman active, especially at low frequency. Examples are the peaks at 124 cm^{-1} (A_u), 151 cm^{-1} (A_u), and 184 cm^{-1} (A_u) in the IR spectrum shown in Figure 3.2, against the 151 cm^{-1} and 184 cm^{-1} vibrational lines in the Raman spectrum presented in Figure 3.1. Other A_u –type of vibrations (dominant transverse optical modes from light interaction with the dipolar moment vector) are observed in the infrared transmission spectrum at 215 cm^{-1}, 276 cm^{-1}, 320 cm^{-1}, 386 cm^{-1}, 440 cm^{-1}, 505 cm^{-1}, and 542 cm^{-1}. Similar to Raman modes, a dominance of those from Bi displacements are expected at low frequency, with that arising from O displacements at high frequency.

3.2 TiO_2

Titanium dioxide has two tetragonal stable phases, anatase and rutile. While both can be encountered at room temperature, the rutile phase prevails at high temperatures, as the anatase phase is known to convert to it at temperatures higher than 750 ^0C [46]. The anatase phase, with the Raman spectrum presented in Figure 3.3, belongs to the space group D^{19}_{4h} ($I4_1/amd$) and exhibits an elongated cell that contains two primitive TiO_2 units. It also consists of octahedral chains/units of TiO_6. All of the six predicted Raman active modes [46] are observed in Figure 3.3, namely the antisymmetric vibrations at 144 cm^{-1} (E_g), 198 cm^{-1} (E_g), and 637 cm^{-1} (E_g), the sharp peaks at 398 cm^{-1} (B_g) and 515 cm^{-1} (doublet from A_{1g} and B_{1g}), and the weak band at 796 cm^{-1} (overtone of B_{1g}). Other weak features indicating disorder induced due to second-order scattering are around 320 cm^{-1} and 448 cm^{-1}. The latter vibration at 448 cm^{-1} (E_g) becomes strong in the rutile phase, as well as the ones at 144 cm^{-1} (B_{1g}) and 612 cm^{-1} (A_{1g}). Another Raman signature of the rutile phase is a peak around 827 cm^{-1} (B_{2g}). In addition, it has been reported the appearance of a broad band around 235 cm^{-1}, which again was associated with disorder induced in the material

[46]. Similar to the Bi_2O_3 case, the low- and mid-frequency regions are dominated by either the Ti–Ti or Ti–O vibrations, respectively.

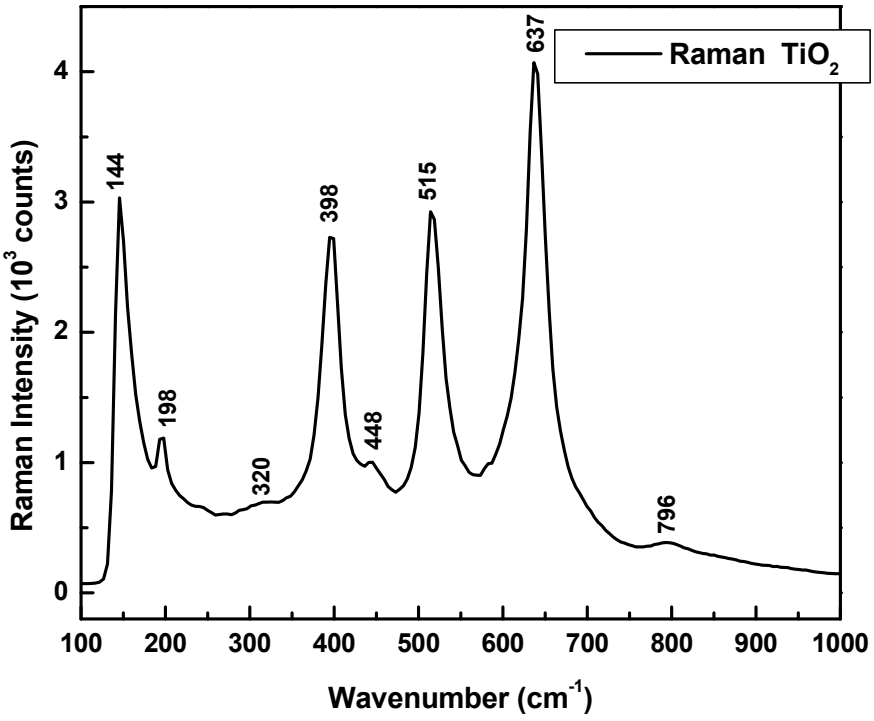

Figure 3.3: Raman spectrum of anatase phase of TiO_2.

The IR spectrum of anatase is presented in Figure 3.4. The transverse optical (TO) and longitudinal optical (LO) modes of titanium dioxide depends on the polarization of light [47,48]. For parallel-polarized light, the A_{2u} modes are active, and for perpendicularly polarized light, the E_u modes are active. Since current measurements do not involve polarization, we were able to observe both types of modes. Thus, the vibrational lines at 268 cm^{-1} (E_u) and at 346 cm^{-1} (A_{2u}), as well as those at 515 cm^{-1} (E_u) and at 637 cm^{-1} (A_{2u}) are all associated with TO modes but belonging to different polarizations of light. Considering the fact that the current measurements were performed using powder samples, the observed shifts of ± 8 cm^{-1} for the mid-IR region are expected when compared with the same values for measurements on crystals [47]. Furthermore,

their increased absorbance is associated with the bulk reststrahlen region between the TO and LO modes.

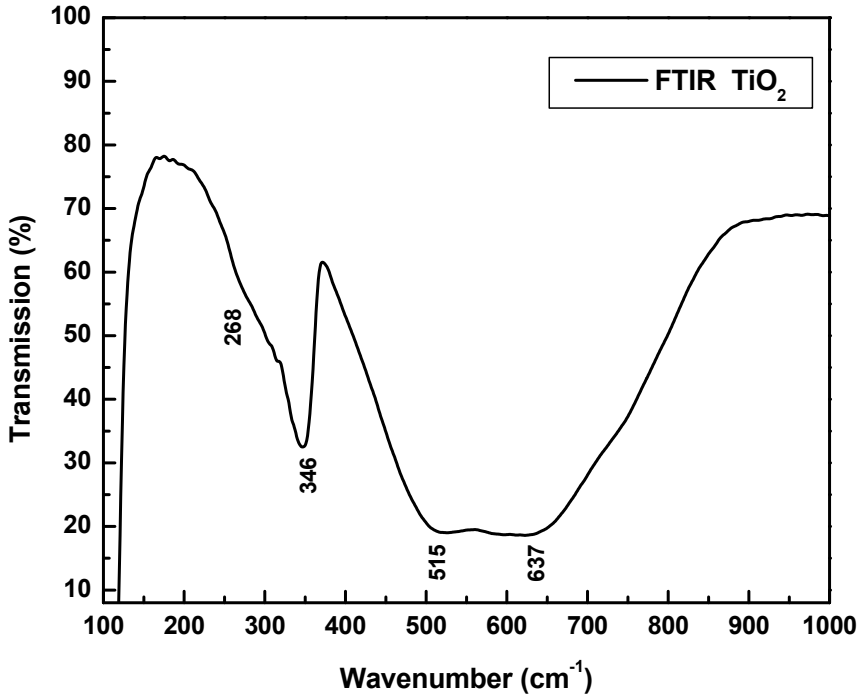

Figure 3.4: Transmission spectrum of anatase phase of TiO_2.

3.3 Fe_2O_3

Between the known iron oxide polymorphs: hematite (α-Fe_2O_3), maghemite (γ- Fe_2O_3), and magnetite (Fe_3O_4), the hematite is the most thermodynamically stable. Long-time exposure to air or heating process results in the conversion of the metastable magnetite and maghemite forms to hematite. The Raman spectrum of iron oxide presented in Figure 3.5 shows dominant peaks at 217 (A_{1g}) and 275 cm^{-1} (E_g) and broad bands at 387 (E_g), 592 (E_g), and 1281 cm^{-1} (overtone or two-phonon) [49,50]. A very weak vibrational line can also be observed at 487 cm^{-1} (A_{1g}). All of these observed vibrations are consistent with those reported for hematite. Furthermore, the absence of the Raman feature around 660 cm^{-1} (LO E_u, Raman forbidden) attributed to the potential residual

presence of other iron oxide forms validate our assumption of hematite existence. The peak at 1281 cm^{-1} has been also associated with magnon scattering besides the two-phonon scattering of the silent mode at 660 cm^{-1} [50].

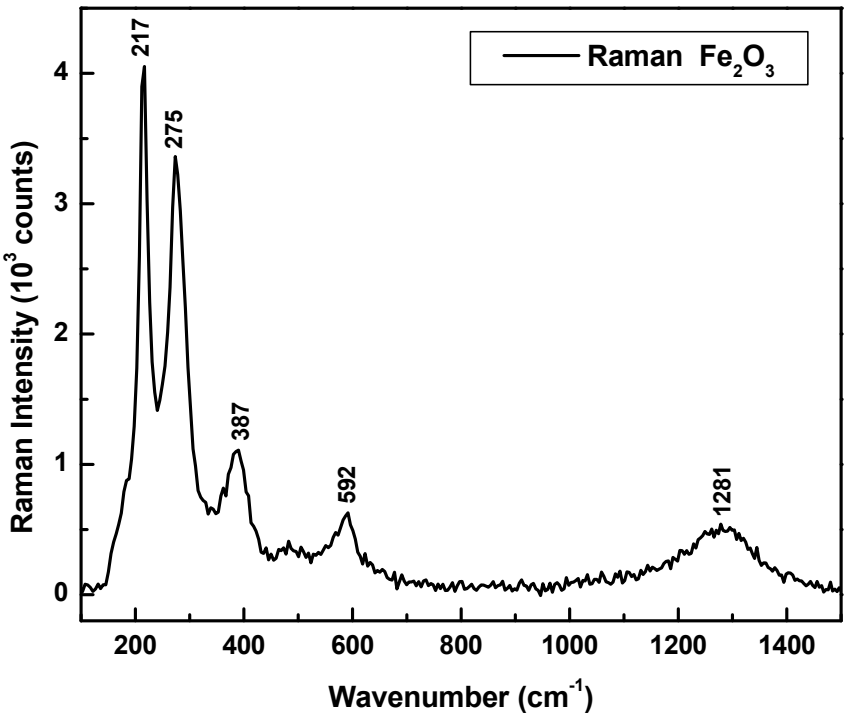

Figure 3.5: Raman spectrum of hematite phase of Fe_2O_3.

The infrared absorption spectrum presented in Figure 3.6 (in a transmission mode) shows vibrational lines at 347, 474, and 550 cm^{-1}, which are in good agreement with the literature reported results [51,52]. The anharmonicity, size, and shape effects characteristics to powder samples contribute to the broadening observed for these vibrations. They also contribute to the weak vibration at 230 cm^{-1} that is becoming experimentally observable for oblate microcrystalline shape. In addition, iron oxide is sensitive to polarization effects as well. To this end, the observed vibrational lines in the IR spectrum are attributed to a perpendicular polarization of light. This is anticipated somehow, as the transverse modes associate with the dipolar moment and dominate

usually in the IR. Other observations are the shoulder around 410 cm^{-1} and the tail at higher frequency of the 550 cm^{-1} peak, both indicating smeared out contributions from parallel polarized light.

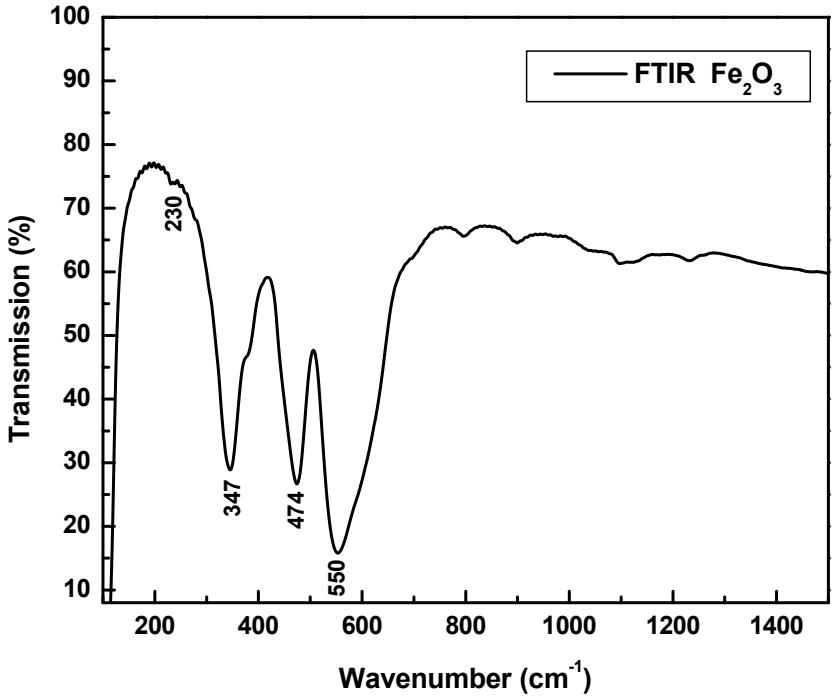

Figure 3.6: Transmission spectrum of hematite phase of Fe_2O_3.

3.4 $Bi_5Ti_3FeO_{15}$

A schematic representation of an aurivillius compound such as $Bi_5Ti_3FeO_{15}$ is presented in Figure 3.7. This perovskite layer material contains A- and B- sites. The B-site corresponds to the octahedral site present in the compound, which is the space at the center of the octahedron, as shown in Figure 3.7. This site is made up of six oxygen molecules where an Fe or Ti atom resides at the center and are disorderly distributed with a 1 to 3 ratio throughout the compound. The A-site is related to the center of the cubic array of the FeO_6/TiO_6 octahedra, where a Bi atom can be found. This array makes up the perovskite structure-like layers found in the aurivillius compound.

The $Bi_5Ti_3FeO_{15}$ structure consists of four perovskite-like layers separated by the fluorite-like $Bi_2O_2^{-2}$ layers. Figure 3.7 shows the layered structure where the blue spheres represent Bi atoms, and the red spheres represent oxygen atoms. The light blue areas represent the FeO_6/TiO_6 octahedra.

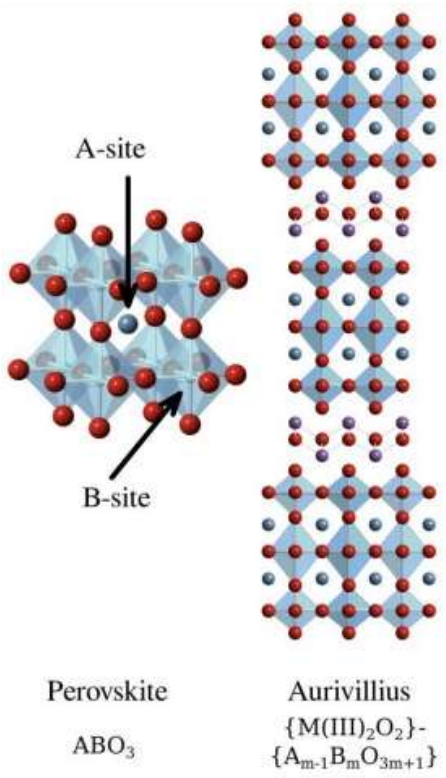

Figure 3.7: Representation of the perovskite A-site in an Aurivillius structure [53].

Table 3.1: Raman and FTIR vibrational modes of constituents.

Bismuth Oxide (Bi_2O_3)		Titanate Oxide (TiO_2)		Iron Oxide (Fe_2O_3)	
Raman (cm^{-1})	**FTIR (cm^{-1})**	**Raman (cm^{-1})**	**FTIR (cm^{-1})**	**Raman (cm^{-1})**	**FTIR (cm^{-1})**
--	124(A_u)	144(E_g)	--	217(A_{1g})	--
153(B_g)	151(A_u)	198(E_g)	--	--	230
184(A_g)	184(A_u)	--	268(E_u)	275(E_g)	--
210(A_g)	215(A_u)	320	--	--	347
282(A_g)	276(A_u)	--	346(A_{2u})	387(E_g)	--
314(A_g)	320(A_u)	398(B_g)	--	--	474
--	386(A_u)	448(E_g)	--	--	550
410(A_g)	--	515(A_{1g})	515(E_u)	592(E_g)	--
446(A_g)	440(A_u)	637(E_g)	637(A_{2u})	1281	--
--	505(A_u)	796(B_{1g})	--	--	--
527(B_g)	--	--	--	--	--
--	542(A_u)	--	--	--	--

The Raman spectrum of $Bi_5Ti_3FeO_{15}$ compound is presented in Figure 3.8. The most substantial peak in the spectrum, centered at about 253 cm^{-1}, is composed of a convolution of three vibrational lines associated with the compound's constituents. The three vibrational lines are 206, 257, and 332 cm^{-1}. The 206 cm^{-1} line in Figure 3.8 is shown as a shift from the 210 cm^{-1} peak in α-Bi_2O_3. The 257 cm^{-1} (A_{1g}) vibrational line comes from the 235 cm^{-1} peak in the rutile phase of TiO_2, with the peak seen at 332 cm^{-1} representing the peaks found around 320-360 cm^{-1} present in rutile [46]. The convolution of these lines is representative of the TiO_6 octahedron found in the aurivillius compound. The 856 cm^{-1} (A_{1g}) peak is correlated with the 827 cm^{-1} line found in rutile. The 548 cm^{-1} (A_{1g}) is in close range to the band found in the rutile spectra present at 541 cm^{-1} [54]. The 708 cm^{-1} is found in the γ-Fe_2O_3 spectra at 710 cm^{-1} [55]. Therefore, this vibrational mode seen in Figure 3.8 corresponds to the FeO_6 octahedra.

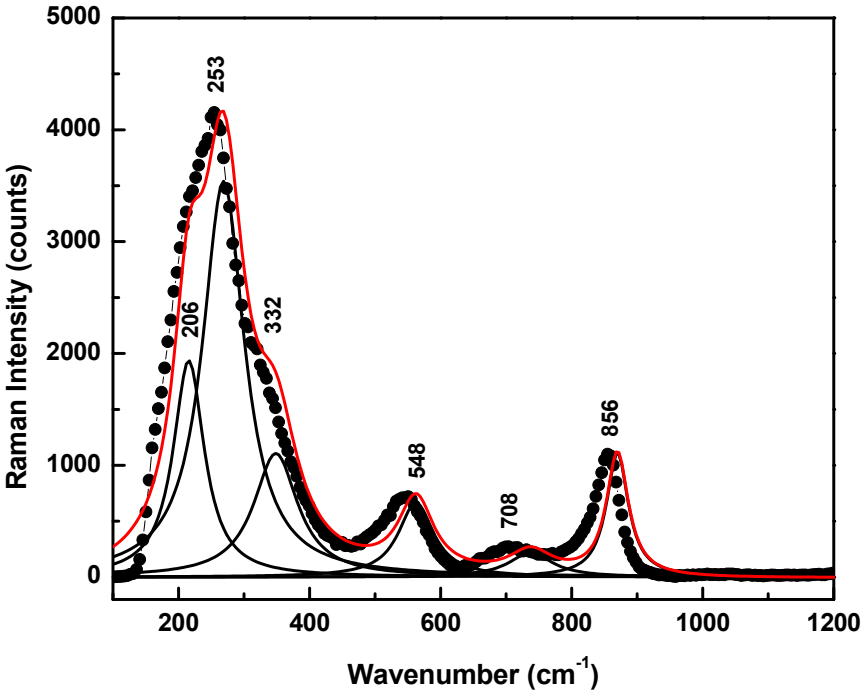

Figure 3.8: Raman spectrum of $Bi_5Ti_3FeO_{15}$ compound.

The spectra found in Figure 3.9 shows the infrared absorption of $Bi_5Ti_3FeO_{15}$. Using Table 3.1, a correlation between each mode can be seen for the constituents and the compound. The vibrational lines seen at 125 and 185 cm^{-1} are in relation to the 124 and 184 cm^{-1} modes present in the FTIR data for Bi_2O_3, where the resolution is given by ±3 for both Raman and FTIR. The peak seen at 303 cm^{-1} is close to the mode seen in Table 3.1 at 314 cm^{-1} belonging to the Raman mode of Bi_2O_3. The sharp peak seen at 382 cm^{-1} comes from FTIR mode at 386 cm^{-1} in Bi_2O_3 and the Raman mode at 387 cm^{-1} in Fe_2O_3. The lines at 435 and 506 cm^{-1} are closer to the modes present in the FTIR spectrum of Bi_2O_3 at 440 and 505 cm^{-1}, respectively. The vibrational line around 558 cm^{-1} is closely related to the line seen in the FTIR spectra for Fe_2O_3 at 550 cm^{-1}. The lines at 612 and 839 cm^{-1} in Figure 3.9 are seen in the Raman spectra for rutile at 612 and 827 cm^{-1}, while the mode at 630 cm^{-1} is correlated to the 637 cm^{-1} mode seen in Table 3.1 under both Raman and FTIR modes of anatase.

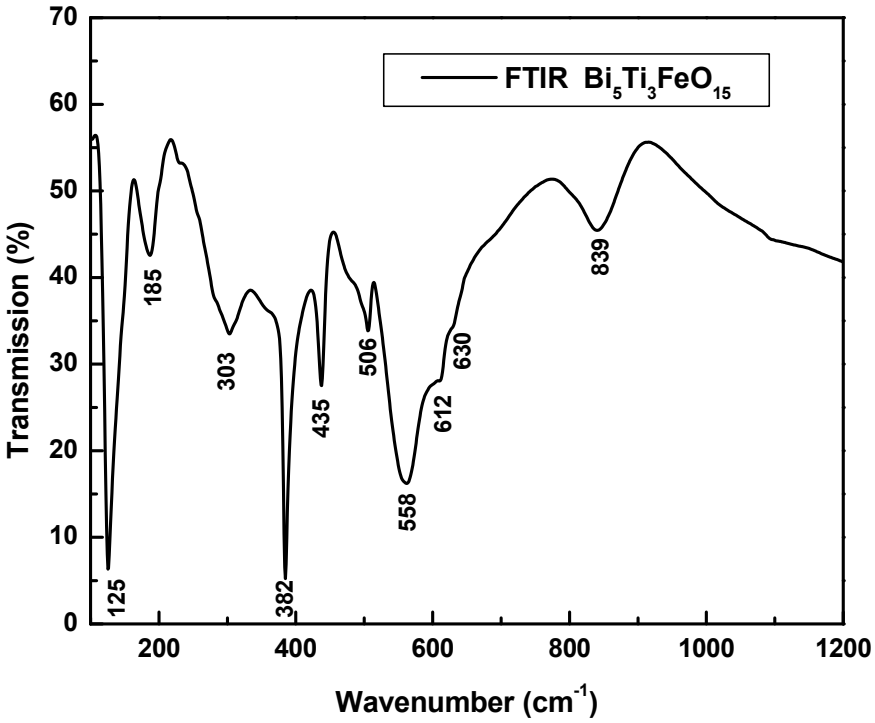

Figure 3.9: Infrared transmission spectrum of $Bi_5Ti_3FeO_{15}$.

In Figure 3.10, we present the powder X-ray diffraction data, which were provided by Dr. Nair in effort of complementing the current spectroscopic analysis. The data demonstrates the orthorhombic structural composition of the Bi5Ti3FeO15 compound. However, a controversial structural change from orthorhombic to tetragonal has been predicted at the currently employed temperature of synthesis. Unfortunately, if observable, it can be seen only at small scattering angles, such as those below 15 degrees. This region is less emphasized in Figure 3.10.

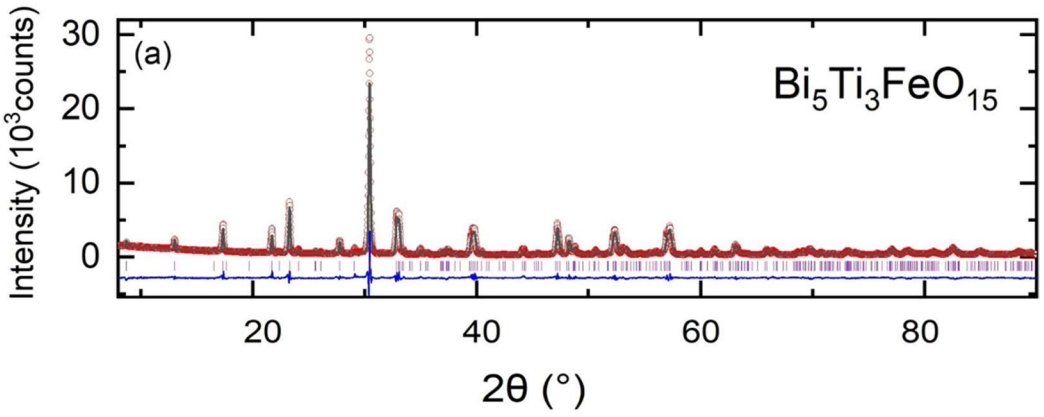

Figure 3.10: Powder X-ray scattering data of the $Bi_5Ti_3FeO_{15}$ compound (courtesy of Dr. Nair).

Conclusion and Future Work

The focus of this study started with $Bi_5Ti_3FeO_{15}$ due to its multiferroic properties and extensive applications. The spectroscopic results of this aurivillius $Bi_5Ti_3FeO_{15}$ phase were analyzed along with those of its constituents, Bi_2O_3, TiO_2, and Fe_2O_3, to show if there were any changes in the structure. Based on these characterizations, the quality of the material is determined to be ideal.

The motivation to study $Bi_5Ti_3FeO_{15}$ comes from the semiconductive, ferroelectric, and antiferromagnetic properties at room temperature. The manipulative magnetic states present in the compound and the mentioned qualities are preferred for specific technological applications. The utilization of this material involves information storage, quantum controlling, and signal processing, to name a few. Furthermore, applying the compound involves its functionality as a gas sensor for detecting harmful gasses. This lead-free compound is also favorable due to its lower toxicity and environmental friendliness.

The study was initiated using the solid-state method to synthesize the aurivillius $Bi_5Ti_3FeO_{15}$ phase material. The compound and its constituents were then analyzed spectroscopically using confocal Raman and vacuum-based Fourier transform infrared spectroscopy. The systems are coupled in this study since both longitudinal and transverse optical modes were required, each being dominant in Raman and FTIR, respectively. The inclusion of the spectra of each constituent was necessary for analyzing the shifts found in the vibrational lines.

From the Raman and FTIR spectra seen for Bi_2O_3, it can be concluded that the lower vibrational lines, at 124, 151, and 184 cm^{-1}, dominate LO modes, given that they are present in both spectra. Higher modes were identified as LO or TO modes, as they were found in the Raman and FTIR spectra, respectively. Vibrational modes found in the Raman spectra below 200

cm^{-1} were identified as belonging to the displacement of Bi and O atoms in the material, while anything higher pertained to Bi-O symmetric bond stretching. In FTIR readings, the lower modes were dominated by Bi displacements, while the higher modes belonged to O displacements.

The stable anatase phase for titanium dioxide was used for this study as it is stable at room temperature. The Raman spectra showed all six expected modes with lower readings correlated to Ti-Ti vibrations and mid-frequency regions assigned to Ti-O vibrations. Since rutile is stable at high temperatures, as experienced during the synthetization of $Bi_5Ti_3FeO_{15}$, the modes at 612 and 827 cm^{-1} must be considered when analyzing the compound. The broad band found in the FTIR spectra around 515-637 cm^{-1} is correlated to the Reststrahlen band, referring to the wavelength region between LO and TO modes with high reflectivity and strong absorption.

Since hematite is known as the most thermodynamically stable phase of iron oxide, it is expected that the modes found in the Raman spectra for Fe_2O_3 correlate with those reported for hematite. Besides all modes associated with hematite, the mode seen at 1281 cm^{-1} correlates to the two-phonon scattering of the silent mode at 660 cm^{-1}. This silent mode further enforces the identification of hematite in the sample. Since Fe_2O_3 is sensitive to polarization effects, FTIR readings will show dominant TO modes.

The modes of importance found in both the Raman and FTIR spectra are summarized in Table 3.1, which is used to analyze $Bi_5Ti_3FeO_{15}$ modes. The modes found in rutile are seen in the Raman spectra, which is evidence of a change in the structure during the synthesis of the compound. A vibrational line in maghemite is also identified in the Raman spectra, further showing the structural change from hematite to maghemite. The modes seen in the low-frequency region of the FTIR spectra are correlated to the modes found in both Raman and FTIR

spectra for Bi_2O_3. The mode is seen at 612 and 630 cm^{-1} is also present in the Raman spectra of rutile, pertaining to the TiO_6 octahedra. The mode at 550 cm^{-1} is correlated to Fe_2O_3 since the same mode is seen in the IR modes. No additional modes were identified.

These assumptions are made by analyzing each constituent's spectra found in this study. Vacuum-based FTIR spectroscopy measurements of pure $Bi_5Ti_3FeO_{15}$ have yet to be reported enough to compare these results. Future work would include density functional theory evaluation. DFT will be used to analyze the information stored in the spectra of the compound.

In addition to Raman and IR, inelastic neutron scattering spectroscopy can measure the collective motions in crystals. This information will identify the magnetism, phase transition, as well as thermodynamic properties of the material. This technique complements the information found in this study as it does not restrict the type of modes allowed, including the high-frequency region (terahertz). This future work would only improve our knowledge of this compound.

In conclusion, a structural change was seen and identified in the spectra of $Bi_5Ti_3FeO_{15}$ compound through confocal Raman and vacuum-based Fourier transform infrared spectroscopy. These results were analyzed by comparing the vibrational spectra of the compound's constituents. The analysis of the material showed no abnormalities suggesting the desired quality of the material.

References

[1] Mazurek, Mariusz & Jartych, Elizabeth & Oleszak, D. (2012). Mössbauer studies of Bi 5Ti 3FeO 15 electroceramic prepared by mechanical activation. Przeglad Elektrotechniczny. 88. 256-258.

[2] Spaldin, N.A., Ramesh, R. Advances in magnetoelectric multiferroics. *Nature Mater* **18,** 203–212 (2019).

[3] Jieyu Chen, Yulong Bai, Chenghong Nie, Shifeng Zhao. Strong magnetoelectric effect of Bi4Ti3O12/Bi5Ti3FeO15 composite films. Journal of Alloys and Compounds. Volume 663. 2016. Pages 480-486.

[4] Rymarczyk, J & Dercz, Grzegorz & Ilczuk, Jan. (2008). Processing, Microstructure and Dielectric Properties of the Bi5Ti3FeO15 Ceramic. Acta Physica Polonica A. 114. 10.

[5] Sun, S.; Yin, X. Progress and Perspectives on Aurivillius-Type Layered Ferroelectric Oxides in Binary Bi4Ti3O12-BiFeO3 System for Multifunctional Applications. Crystals 2021, 11, 23. https://doi.org/10.3390/cryst11010023

[6] K. Laurent, G.Y. Wang, S. Tusseau-Nenez, Y. Leprince-Wang. Structure and conductivity studies of electrodeposited δ-Bi2O3. Solid State Ionics. Volume 178, Issues 33–34. 2008. Pages 1735-1739.

[7] Osmary Depablos-Rivera, Ana Martínez, Sandra E. Rodil. Interpretation of the Raman spectra of bismuth oxide thin films presenting different crystallographic phases. Journal of Alloys and Compounds. Volume 853, 2021.

[8] Pereira AL, Gomis O, Sans JA, Pellicer-Porres J, Manjón FJ, Beltran A, Rodríguez-Hernández P, Muñoz A. Pressure effects on the vibrational properties of α-Bi(2)O(3): an experimental and theoretical study. J Phys Condens Matter. 2014 Jun 4;26(22):225401. doi: 10.1088/0953-8984/26/22/225401. Epub 2014 May 9. PMID: 24810681.

[9] Maeder, T. (2013). Review of Bi2O3 based glasses for electronics and related applications. *International Materials Reviews, 58*, 3 - 40.

[10] Gupta, S.M., Tripathi, M. A review of TiO_2 nanoparticles. *Chin. Sci. Bull.* **56,** 1639 (2011).

[11] Cromer D T, Herrington K. The structures of anatase and rutile. J Am Chem Soc, 1955, 77: 4708–470932

[12] Baur V W H. Atomabstände und bindungswinkel im brookit, TiO2. Acta Crystallogr, 1961, 14: 214–21633

[13] Jia, Junjun & Yamamoto, Haruka & Okajima, Toshihiro & Shigesato, Yuzo. (2016). On the Crystal Structural Control of Sputtered TiO2 Thin Films. Nanoscale Research Letters. 11. 10.1186/s11671-016-1531-5.

[14] Adawiya J. Haider, Riyad Hassan AL– Anbari, Ghadah Rasim Kadhim, Chafic Touma Salame. Exploring potential Environmental applications of TiO2 Nanoparticles. Energy Procedia. Volume 119. 2017. Pages 332-345.

[15] Jafari S, Mahyad B, Hashemzadeh H, Janfaza S, Gholikhani T, Tayebi L. Biomedical Applications of TiO2 Nanostructures: Recent Advances. *Int J Nanomedicine*. 2020

[16] Hashemzadeh H, Javadi H, Darvishi MH. Study of structural stability and formation mechanisms in dspc and dpsm liposomes: a coarse-grained molecular dynamics simulation. Sci Rep. 2020;10(1):1837. doi:10.1038/s41598-020-58730-z

[17] Li Q,Wang X, Lu X, et al. The incorporation of daunorubicin in cancer cells through the use of titanium dioxide whiskers. Biomaterials. 2009;30(27):4708–4715. doi:10.1016/j.biomaterials.2009.05.015

[18] Nešić M, Žakula J, Korićanac L, et al. Light controlled metallo-drug delivery system based on the tio2 nanoparticles and ru-complex. J Photochem Photobiol a Chem. 2017;347:55–66. doi:10.1016/j.jphotochem.2017.06.045
[19] Besinis A, De Peralta T, Handy RD. The antibacterial effects of silver, titanium dioxide and silica dioxide nanoparticles compared to the dental disinfectant chlorhexidine on streptococcus mutans using a suite of bioassays. Nanotoxicology. 2014;8(1):1–16. doi:10.3109/17435390.2012.742935
[20] Wang H, Lai Y-K, Zheng R-Y, Bian Y, Zhang K Q, Lin C-J. Tuning the surface microstructure of titanate coatings on titanium implants for enhancing bioactivity of implants. Int J Nanomedicine. 2015;10:3887. doi:10.2147/IJN.S75999
[21] Molaeirad A, Janfaza S, Karimi-Fard A, Mahyad B. Photocurrent generation by adsorption of two main pigments of halobacterium salinarum on tio2 nanostructured electrode. Biotechnol Appl Biochem. 2015;62(1):121–125. doi:10.1002/bab.1244
[22] Sibel AO, Shah A, editors. Nanomaterials based enzyme biosensors for electrochemical applications: recent trends and future prospects. In: New Developments in Nanosensors for Pharmaceutical Analysis. Elsevier; 2019:381–408.
[23] Mohsen Shahrousvand, Monireh Sadat Hoseinian, Marzieh Ghollasi, Ali Karbalaeimahdi, Ali Salimi, Fatemeh Ahmadi Tabar. Flexible magnetic polyurethane/Fe2O3 nanoparticles as organic-inorganic nanocomposites for biomedical applications: Properties and cell behavior. Materials Science and Engineering: C. Volume 74. 2017. Pages 556-567
[24] Arias, L., Pessan, J., Vieira, A., Lima, T., Delbem, A., & Monteiro, D. (2018). Iron Oxide Nanoparticles for Biomedical Applications: A Perspective on Synthesis, Drugs, Antimicrobial Activity, and Toxicity. *Antibiotics*, 7(2), 46. https://doi.org/10.3390/antibiotics7020046
[25] Shan-Shan Li, Wen-Juan Li, Tian-Jia Jiang, Zhong-Gang Liu, Xing Chen, Huai-Ping Cong, Jin-Huai Liu, Yu-Ying Huang, Li-Na Li, and Xing-Jiu Huang. Iron Oxide with Different Crystal Phases (α- and γ-Fe2O3) in Electroanalysis and Ultrasensitive and Selective Detection of Lead(II): An Advancing Approach Using XPS and EXAFS. Analytical Chemistry. 2016. 88 (1), 906-914 DOI: 10.1021/acs.analchem.5b03570
[26] Ferraro, J. R., & Nakamoto, K. (2012). Introductory Raman spectroscopy. Elsevier Science.
[27] WITec Wissenschaftliche Instrumente und Technologie GmbH, U. (n.d.). Raman. Raman || WITec Raman Imaging. Retrieved July 5, 2021, from https://www.witec.de/techniques/raman/.
[28] Sponsored by B&W TekDec 2 2016. (2019, October 22). Raman knowledge - an introduction to Raman spectroscopy. AZoM.com.
[29] Larkin, P. J. (2018). *Infrared and Raman spectroscopy principles and spectral interpretation*. Elsevier.
[30] Ferraro, J. R., Nakamoto, K., & Brown, C. W. (2003). Introductory Raman spectroscopy (2nd ed.). Academic Press.
[31] Butterfly, B. (2019, March 27). *Ftir: Fourier-transform infrared spectroscopy principles and applications*. FindLight Blog.
[32] Guide to FT-IR spectroscopy. Bruker. (n.d.).
[33] Britannica, T. Editors of Encyclopaedia (2020, July 27). Michelson-Morley experiment. Encyclopedia Britannica.
[34] Admin. (2022, June 24). *Fourier transform - definition, formula, properties, applications and examples*. BYJUS.

[35] Eberhardt, K., Stiebing, C., Matthäus, C., Schmitt, M., & Popp, J. (2015). Advantages and limitations of Raman spectroscopy for molecular diagnostics: An update. Expert Review of Molecular Diagnostics, 15(6), 773–787.
[36] Cabot A, Marsal A, Arbiol L, et al, Bi2O3 as a selective sensing material for NO detection. Sens. Actu. B, 2004 99, 74-89.
[37] Hwang GH, Han WK, Park JS, et al. An electrochemical sensor based on reduction of screen-printed bismuth oxide for the determination of lead and cadmium. Sens. Actu. B 2008, 135, 309-316.
[38] Metrolabmarketing. (2019, October 21). *Theory of raman scattering*. Metrolab Blog. Retrieved December 6, 2022, from https://metrolab.blog/theory-of-raman-scattering/
[39] Gou X, Li R, Wang G, et al. Room-temperature solutions synthesis of Bi2O3 nanowires for gas sensing application. Nanotechnology 2009, 20, 495-501.
[40] Hyodo T, Kanazawa E, Takao Y, Shimizu Y, Egashira M. H2 sensing properties and mechanism of Nb2O5-Bi2O3 varistor-type gas sensors. Electrochemistry 2000, 68(1), 24-31.
[41] Senna M. A straight way toward phase pure complex oxides. Journal of the European Ceramic Society 25 (2005) 1977–1984.
[42] Leontie L, Caraman, M, Delibas M, Risu GI. Optical properties of bismuth trioxide thin films. Materials Research Bulletin, 2001, 36, 1629-1637.
[43] Betsch RJ and White WB. Vibrational spectra of bismuth oxide and the selenite-structure bismuth derivatives. Spectrochemica Acta 1977, 34A, 505-514.
[44] Pereira, Gomis et al, Pressure effects on the vibrational properties of α-Bi 2O3: An experimental andtheoretical study. May 2014, Journal of Physics Condensed Matter 26(22):225401
[45] Ling, B.; Sun, X. W.; Zhao, J. L.; Shen, Y. Q.; Dong, Z. L.; Sun, L. D.; Li, S. F.; Zhang, S. One-Dimensional Single-Crystalline Bismuth Oxide Micro/Nanoribbons: Morphology-Controlled Synthesis and Luminescent Properties. Journal of Nanoscience and Nanotechnology, Volume 10, Number 12, December 2010, pp. 8322-8327.
[46] Balachandran U and Eror NG. Raman Spectra of Titanium Dioxide. Journal of Solid State Chemistry 42, 276-282 (1982).
[47] Gonzalez RJ, Zallen R. Infrared reflectivity and lattice fundamentals in anatase TiO2. Phys. Rev. B 55(11), 7014-7017 (1997)
[48] Cromer D T, Herrington K. The structures of anatase and rutile. J Am Chem Soc, 1955, 77: 4708–470932
[49] Jubb A. M, Allen, H.C. Vibrational Spectroscopy Characterization of Hematite, Maghemite, and Magnetite Thin Films Produced by Vapor Deposition. ACS Appl. Materials & Interfaces. 2(10), 2804-2812, 2010.
[50] Sunny A., Thirumurugan A., Balasubramanian K. Laser induced Fano scattering, electron-phonon coupling, bond length and phonon lifetime changes in α- Fe_2O_3 nanostructures. Phys. Chem. Chem. Phys. 22, 2001-2009, 2020.
[51] Hayashi S and Kanamori H. Infrared study of surface phonon modes in α-Fe2O3 microcrystals. Journal of Physics C: Solid State Physics. 13, 1529-1538 (1980).
[52] Wang Y, Muramatsu A, Sugimoto T. FTIR analysis of well-defined α-Fe2O3 particles. Colloids and Surfaces A: Physiological and Engineering Aspects. 134 (1998) 281-297.
[53] Metz, Peter. (2017). Total Scattering Analysis of Disordered Nanosheet Materials. 10.6084/m9.figshare.4896902.

[54] Swamy, V., Muddle, B. C., & Dai, Q. (2006). Size-dependent modifications of the Raman spectrum of rutile Ti O 2. *Applied Physics Letters*, *89*(16), 163118.
[55] Stagi, L., De Toro, J. A., Ardu, A., Cannas, C., Casu, A., Lee, S. S., & Ricci, P. C. (2014). Surface effects under visible irradiation and heat treatment on the phase stability of γ-Fe2O3 nanoparticles and γ-Fe2O3− SiO2 core–shell nanostructures. *The Journal of Physical Chemistry C*, *118*(5), 2857-2866.

Vita

Mariana Castellanos was born in El Paso, Texas. They attended elementary school in the El Paso School District and graduated from Montwood High School with honors in May 2016. The following August they entered the University of Texas at El Paso and in May 2019 received the degree of Bachelor of Science in Medical Physics with Cum Laude honors. They also received teaching experience through the Teacher Assistant program. After a year of working as a personal tutor, they entered the University of Texas at El Paso in August 2020 and received a Master of Science in Physics. They can be contacted through email at mcastellano@miners.utep.edu.